Understanding Interfacial Development and Dynamic Mechanical Properties of Electrophoretically Deposited Graphene Oxide Films on Al Alloy Substrates

Su Min Jin

Master of Science

Department of Mining and Materials Engineering

McGill University, Montreal, QC

July, 2015

A thesis submitted to McGill University in partial fulfillment of the requirements of the degrees of Master of Science

© Su Min Jin, 2015

ABSTRACT

Electrophoretic deposition (EPD) of graphene oxide (GO) has obtained growing attention due to its deposition simplicity and cost-effectiveness. Moreover, EPD is an environmentally friendly process and has easy scaling up possibilities towards large substrate size with almost no limitation in substrate shape. Adhesion between the film and the substrate is critical for functional coating applications and electronic devices as it dictates coating lifetime and electron transport between the two layers. Although, EPD has shown to promote good adhesion of GO on various substrate materials, no in-depth study has been performed on interfacial development or dynamic mechanical behavior of EPD GO films on Al substrates. To overcome this knowledge gap, this thesis proposes to study interfacial chemistry and dynamic mechanical properties of EPD GO films on Al alloy substrates. Al alloys were chosen as substrate materials due to their versatile applications and many advantages including lightweight, abundance, ductility, and good electrical and thermal conductivity. Three different commercially available Al alloys are used in this study, namely Al 1100, Al 5052, and Al 6061. X-ray photoelectron spectroscopy (XPS) with depth profiling and nano-impact testing were primarily employed to investigate chemical and mechanical properties of EPD GO films on Al alloys, respectively. From qualitative adhesion test, no apparent improvement in adhesion was observe with respect to EPD parameters. However, film adhesion was highly affected by composition of substrate materials. From XPS depth profiling results, metal ion penetration into GO films was observed. Moreover, GO films on Al alloy substrates had Al–O–C bond formations from oxygenated defects. From nano-impact testing, crack formation starting from the film surface is observed. From dynamic energy dissipation calculation, GO films displayed exceptional ability to dissipate high impact energy per density.

ABRÉGÉ

Le dépôt par électrophorèse (EPD) d'oxyde de graphène (GO) a obtenu une attention croissante du fait de la simplicité de l'appareillage et de la rentabilité. En outre, EPD est un processus non polluant, permet facilement d'augmenter la dimension des substrats, et n'a pas de limitation de forme. L'adhérence entre les films et les substrats est critique pour les applications de revêtements fonctionnels et des appareils électroniques, car elle contrôle la durée de vie des revêtements et le transport d'électrons entre les deux couches. Bien que le EPD favorise une bonne adhérence de GO sur divers matériaux formant les substrats, l'étude des propriétés chimiques interfaciales ou du comportement mécanique n'a pas été effectuée. Pour surmonter cette lacune du connaissance, cette thèse propose d'étudier les propriétés chimique et mécanique des films EPD GO sur les alliages d'aluminium comme substrats. Les alliages d'aluminium ont été choisis comme matériaux de substrats du fait de leurs polyvalence au niveau des applications et d'avantages tel que, y compris la légèreté, l'abondance, la ductilité, et une bonne conductivité électrique et thermique. Trois différents alliages d'aluminium qui sont disponibles commercialement sont utilisés dans cette étude, à savoir Al 1100, Al 5052, et Al 6061. La Spectrométrie photoélectronique X (XPS) et le Nano-impact ont été principalement utilisée pour étudier les propriétés chimique et mécanique des films EPD GO sur les alliages d'aluminium. Des tests qualitatifs d'adhérence n'ont montré aucune amélioration de l'adhérence à l'égard des paramètes de l'EPD. Par contre, l'adhérence a été influencée par la composition des matériaux de substrats. Des analyses XPS en profondeur ont permi l'observation d'une pénétration d'ion métallique dans les films GO. En outre, les films GO sur substrats en alliage d'aluminium ont montré la formation de défauts oxygénés avec liaisons Al–O–C. De tests Nano-impact ont permi d'observer la formation de fissures à partir de la surface du film. Des calculs dynamiques dissipation d'énergie ont permi d'établir une capacité exceptionnelle des films GO à dissiper des valeurs élevées d'énergie d'impact normalises à la densité.

ACKNOWLEDGEMENTS

First and foremost, I would like to express my sincere gratitude to Professor Mathieu Brochu and Professor James H. Dickerson for their supervision throughout the project. Their guidance and encouragements not only kept me on the right track but also helped me to improve my research skills and prepared me to be a better researcher. I also thank them for their time and effort to review the manuscripts and this thesis.

I would like to acknowledge Dr. Viet Hung Pham for contributing his time and effort in this project. I am most grateful for his help on experiments and valuable advices through out the project. I want to thank him for reviewing the manuscripts and providing suggestions to improve quality of the paper.

I would like to thank all members of P^2AM^2 Lab and Dr. Dickerson' research group. I feel lucky to work in both groups. I especially thank Jason and Walker for their time and effort to review and comment research presentations related to the project during my Master study. I would also like to thank Javier and Abhi for their work to maintain good experimental environment for our lab machine.

I would like to thank McGill University, Aluminum Research Centre – REGAL, Fonds de Recherche Quebec Nature et Technologies – FQRNT, and US Department of Energy for their financial support for this project.

Finally, I would like to extend my deepest gratitude to my family and friends for their continuous support and encouragements during my study.

CONTRIBUTIONS

This thesis is written as a collection of two manuscripts:

1. *Understanding interfacial development of electrophoretically deposited graphene oxide films on Al alloys*

2. *Dynamic mechanical characterization of electrophoretically deposited graphene oxide films on Al 5052 substrates*.

The role of each contributor is as follow:

- **Miss Su Min Jin** primarily performed all experiments, data collection, and analyses except for GO synthesis, and is the primary author of both manuscripts.

- **Dr. Viet Hung Pham** is co-author of both manuscripts due to his contribution in GO synthesis and providing valuable advices and help through out the film deposition process and chemical analyses of the specimens.

- **Professor Mathieu Brochu** and **Professor James H. Dickerson** are co-authors in both manuscripts in their contribution as the research supervisors.

- **Mr. Abhi Ghosh** is designated as a co-author of the second manuscript due to his contribution in mechanical data analysis.

TABLE OF CONTENTS

LIST OF FIGURES

LIST OF TABLES

CHAPTER 1

Introduction

With increasing demand for smaller and lighter devices for electronic, energy harvesting, and biomedical applications, research in nanomaterials have grown rapidly over the past years. Materials in nanometer scales tend to have superior electronic, thermal, and mechanical properties than in their bulk form. Carbonateous nanomaterials including carbon nanotubes (CNTs), fullerene, and graphene are especially propitious due to abundant source of carbon [1.1]. Graphene is a planar monolayer of hexagonally structured carbon atoms and a basic building block of fullerene, carbon nanotube, and graphite [1.2]. Figure 1–1 portrays structures of carbonateous nanomaterials made from the building block [1.2].

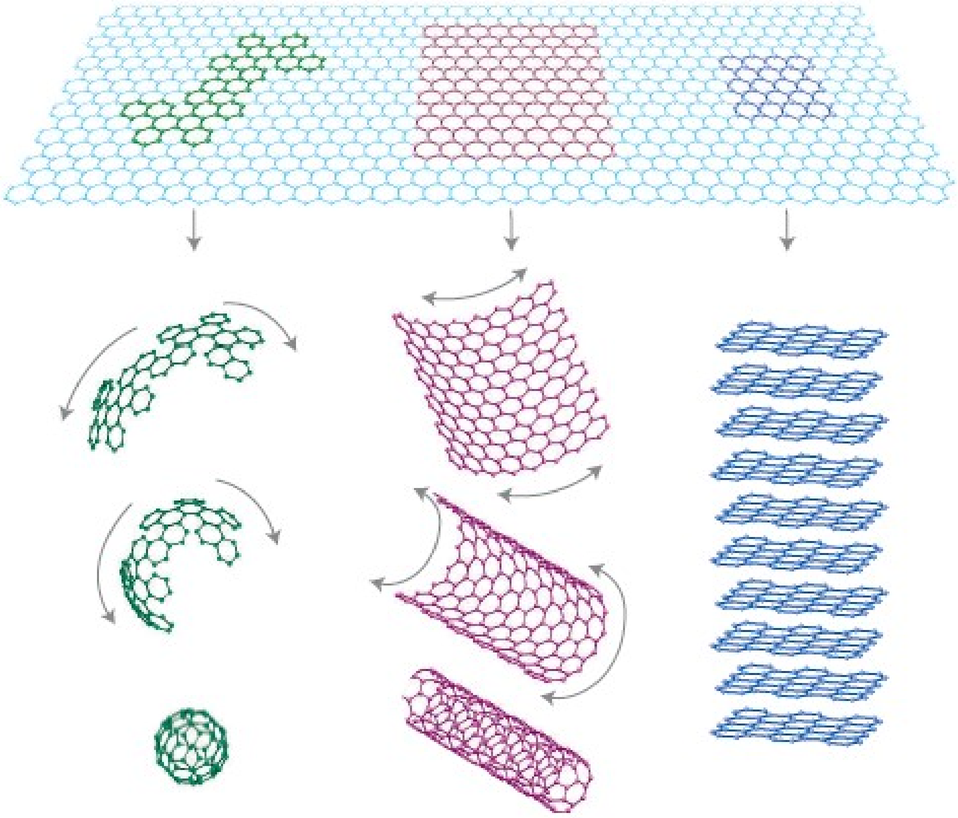

Figure 1–1. Schematic diagram of structures derived from planar graphene [1.2].

Planar graphene has been a particular interest to many scientists because of its two-dimensional structure and high aspect ratio (lateral size to thickness) [1.3]. Its extremely high electron mobility at room temperature (250,000 cm^2/Vs) [1.4, 1.5], excellent thermal conductivity (5000 $Wm^{-1}K^{-1}$) [1.6], superior compressive elastic modulus of 1 TPa [1.7], and chemical inertness [1.8] make an ideal material for applications including transparent optoelectronic devices, field effect transistors, gas sensors, and corrosion-inhibiting coatings [1.5, 1.9-1.12]. In addition, relatively low production cost with better materials properties than CNTs make it a promising material for scalable devices [1.13]. This chapter contains reviews of the current state in graphene-based materials synthesis and their mechanical properties followed by motivations and objectives of the thesis project.

1.1 Graphene Production

1.1.1 Chemical and mechanical exfoliation

Before a prominent discovery by Geim and Novoselov in 2004, planar graphene was presumed to be thermodynamically unstable to exist in monolayer form [1.5]. Mechanical cleavage technique developed by Novoselov and co-workers has opened up a new chapter of producing graphene monolayers for materials characterization and actual device applications [1.5]. Few atomic layers of graphitic sheets, including single layer, have been successfully fabricated by scotch taping of highly oriented pyrolytic graphite (HOPG). To explain this process briefly, 1 mm thick platelet of HOPG is dry etched by oxygen plasma to produce 5 μm–deep mesas. Mesas are square shaped valley. Using nano–imprint lithography technique, the structured surfaces are pressed against 1 μm–thick photoresist spun on glass substrates and subsequently baked for curing. Prepared HOPG platelets supported by the photoresist are then mechanically cleaved using repeated scotch tape peels. Finally, photoresist layer is removed in acetone to release thin layers of graphene. Freestanding few layers graphene is captured on Si wafer surface with the aid of Van der Waals and capillary forces for further characterizations. Figure 1–2 shows a photo of mechanically exfoliated graphene films using scotch tape peel. The produced films had lateral size of up to 10 μm. Lateral size of up to 100 μm was achieved for films thicker than 3 nm.

Mechanical cleavage of HOPG is considered as the most reliable method to produce high-purity graphene monolayer and has been used for most of experimental characterizations [1.2]. However, the technique is not suitable for processing bulk quantity due to low production.

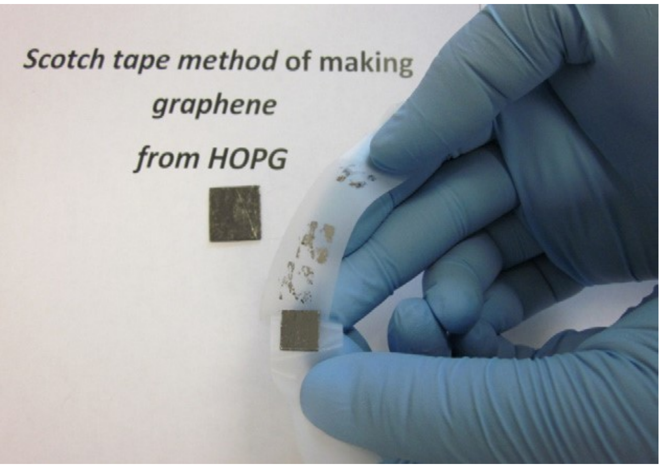

Figure 1–2. Photograph of mechanical cleavage technique using scotch tape peel [1.13].

A number of alternative approaches have been taken to produce large quantity of few layer graphene films using chemical exfoliation. The key challenge in producing single layer of graphene is aggregation, which is a common challenge in bulk production of nanomaterials [1.13]. Hernandez *et al.* used N–methyl–pyrrolidone (NMP) to exfoliate a few layer of graphene [1.14]. NMP can stabilize exfoliated graphene by solvent–graphene interactions. The surface energy of NMP matches that of graphene and balances the energy required to exfoliate graphene layers. However, the use of NMP is limited by its high cost and high boiling temperature [1.13]. Another approach is to use surfactants to encapsulate single layer and few layer graphene during ultrasonication of graphite in water. Adsorbed surfactants produce graphene–surfactant complexes, which are stabilized by coulomb repulsion force in water [1.15]. Surfactants including sodium dodecylbenzene sulfonate (SDBS) [1.15], and sodium cholate (SC) [1.16] were successful in encapsulating few layer graphene flakes. The resulting suspension consisted of large quantity of multi–layer graphene below 5 layers in thickness but only small quantity of monolayer graphene could be obtained. Figure 1–3 displays a schematic diagram explaining graphene flake encapsulation by surfactants. Simultaneous process of chemical exfoliation, reintercalation, and expansion of graphite has successfully produced stable suspensions of single layer graphene sheets in organic solvents [1.17]. Graphitic intercalation compounds (GISs), commonly known as expandable graphite, has small molecules or polymers non-covalently attached between layers of graphite [1.13]. The small molecules in between the layers assist in separating single layers of graphene. Li *et al.* intercalated chemically exfoliated graphene using tetrabutylammonium hydroxide (TBA) then coated graphene layers in N,N–dimethylformamide (DMF) solution with phospholipid–polyethyleneglycol (PEG) complexes [1.17]. Figure 1–4 depicts the process. From this, single layers of graphene sheets were obtained. Although, chemical exfoliation techniques produce larger quantity of graphene sheets than mechanical cleavage, attachment of foreign substance is often considered to be undesirable [1.18]. In addition, complexity in multiple process steps is another drawback.

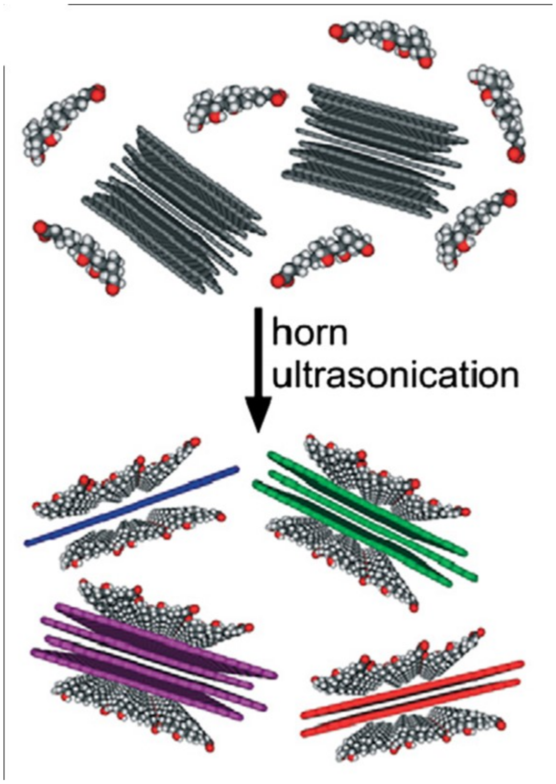

Figure 1–3. Schematic diagram of graphene encapsulation in surfactants [1.16].

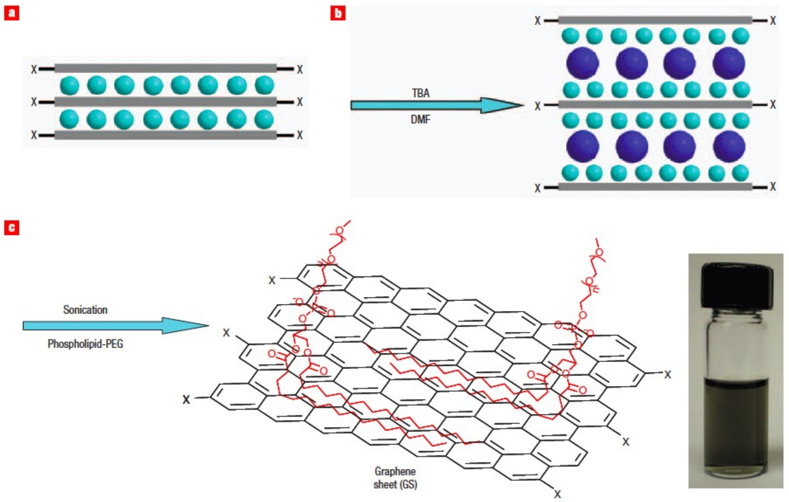

Figure 1–4. Process diagram for exfoliation and re-intercalation technique and resulting liquid suspension [1.17].

1.1.2 Epitaxial growth and chemical vapor deposition (CVD) processes

Pristine graphene films were obtained by epitaxial growth on SiC substrates by Berger *et al.* [1.19]. Vacuum graphitization reaction of carbon atoms enables growth of transfer–free graphene films directly on the SiC substrates. In essence, surface Si atoms are removed by sublimation upon heating in ultra high vacuum (UHV). The leftover surface carbon atoms then rearrange into a form of graphene. This process is useful in the semiconductor industry because Si is a commonly used substrate and direct deposition can avoid defects in the graphene films during lift–off and transfer process. On the other hand, requirement of UHV is a major drawback. Chemical vapor deposition (CVD) is an emerging technique for large–area production of high purity transferrable graphene films. Somani *et al.* successfully synthesized of few-layer graphene films using CVD for the first time in 2006 [1.20]. They used camphor as a precursor to deposit graphene films on Ni foil substrates. Since then, graphene films has deposited primarily on Ni [1.10, 1.21-1.23] and Cu [1.21, 1.24] substrates using CVD. The carbon solubility in the substrates affects the graphene growth mechanism [1.21, 1.24]. Ni is known for high carbon solubility, whereas, Cu has low carbon solubility. In–depth study performed by Li *et al.* using carbon isotope labeling and Raman spectroscopy has revealed that the graphene growth on Cu is carried out by surface catalyzed process rather than precipitation process, which is the case for

Ni [1.21]. Figure 1–5 illustrates the two different processes. The surface catalyzed process explained by Li and co-workers are divided into four steps. First, methane gas is catalytically decomposed on metal substrates to form C_xH_y species on the surfaces. Depending on the growth temperature, methane pressure and flow, and partial pressure of hydrogen, the saturation level of C_xH_y species on the surface changes. Nuclei start to form on the surface due to local supersaturation of C_xH_y followed by nuclei growth to form graphene islands on the metal surface. Finally, depending on the amount of C_xH_y available at the surface, the surface will be fully or partially covered by graphene islands. Low carbon solubility of the substrate yields self-limited growth process, which is favorable in terms of producing single layer graphene. Larger grain size was obtained for films grown on Cu compared to films grown on high carbon solubility metal substrates like Ni and Co [1.24]. In the precipitation process, graphene films are produced by diffusion of carbon atoms into metal substrates at growth temperature followed by subsequent precipitation of carbon atoms upon rapid cooling of the substrates. The cooling forces out–diffusion of carbon and the precipitated carbon atoms form an ordered layer of graphene.

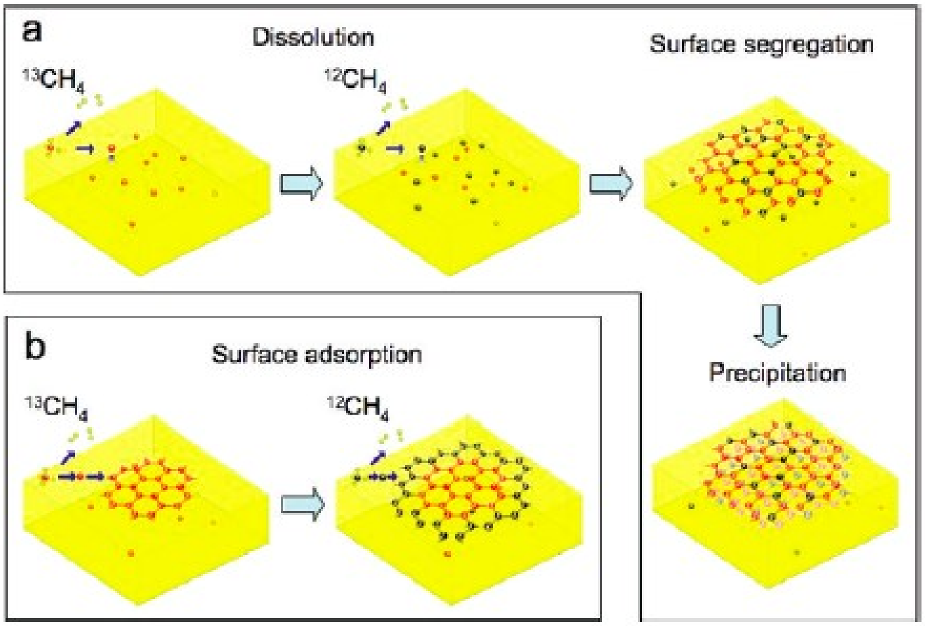

Figure 1–5. Schematic diagrams of CVD growth mechanisms – (a) precipitation process and (b) surface catalyzed process [1.21].

In order to obtain high–quality graphene films, the substrate–cooling rate is critical. Yu *et al.* experimented with three different cooling rates; fast (20 °C/s), medium (10 °C/s), and slow (0.1 °C/s) [1.23]. They obtained good quality film at the medium rate. In contrast, films were poorly formed at fast rate due to the lost of carbon atom mobility and at slow rate due to absence of carbon atom segregation. Figure 1–6 depicts carbon atom diffusion and precipitation processes with respect to cooling rate. Despite its efficiency to mass–produce high purity transferrable graphene films, CVD is limited by the need of sophisticated instrument and substrate selectivity. Defects are most likely to be introduced during the lift–off and transfer process. Transferred films tend to have poor adhesion to the substrates and interfacial defects weaken device performance. Therefore, selectivity of substrate material makes these techniques unsuitable for functional coating applications for a large range of substrate materials.

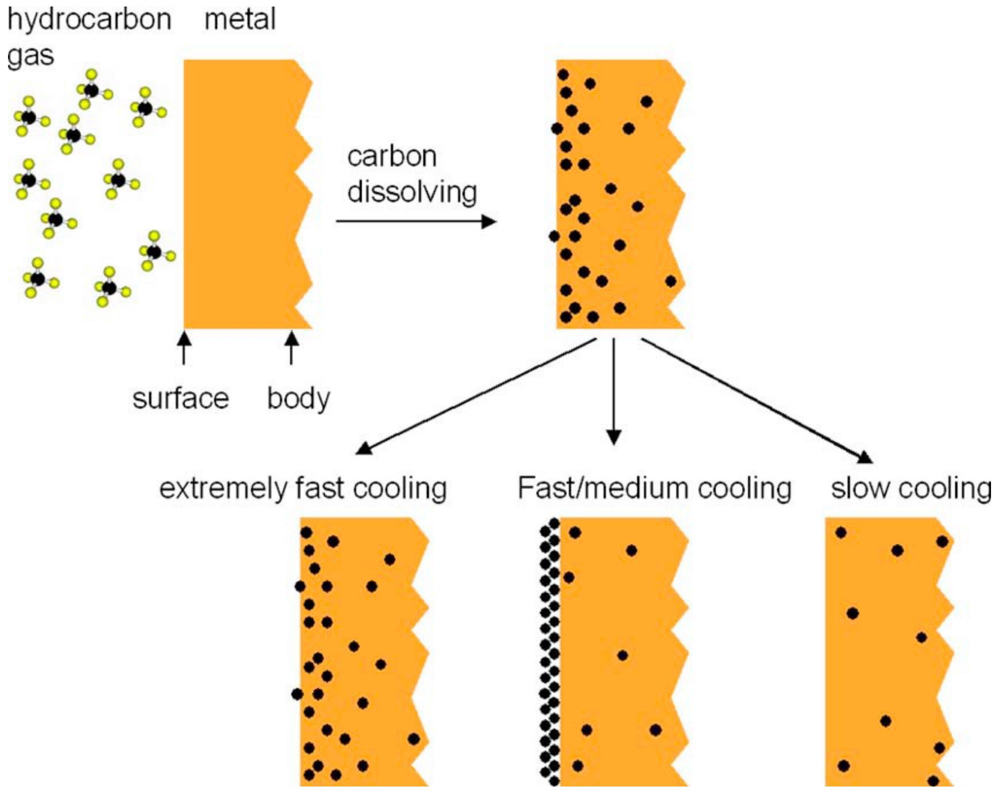

Figure 1–6. Diagram explaining movement of adsorbed carbon atoms with respect to substrate cooling rate [1.23].

1.1.3 Chemically derived graphene

Chemical conversion technique using graphite oxide as a precursor material is an efficient approach to produce bulk quantity of graphene–based material at low cost [1.18]. Graphite oxide can be produced using concentrated sulfuric acid, nitric acid and potassium permanganate based on method developed by Hummers and Offeman [1.25]. Oxidation of graphite creates oxygenated defects on the surfaces of graphite sheets and increases interlayer distances, which is favorable for single layer exfoliation. In addition, hydrophilic characteristic of graphite oxide enables exfoliation and dispersion of single layer sheets in aqueous media. The defects can be partially removed by subsequent chemical treatment using hydrazine [1.26] and sodium borohydride [1.27] or thermal reduction process.

Structures of pristine graphene and chemically derived graphene are different due to oxygenated defects. Single layer derived from graphite oxide is called graphene oxide (GO) and those reduced chemically or thermally are often referred as reduced GO. From multiple solid–state nuclear magnetic resonance (SSNMR) studies, models of GO structure have been proposed [1.28-1.31]. Figure 1–7 gives a structure model from Gao and co-workers [1.29] based on Lerf-Klinowski model [1.31].

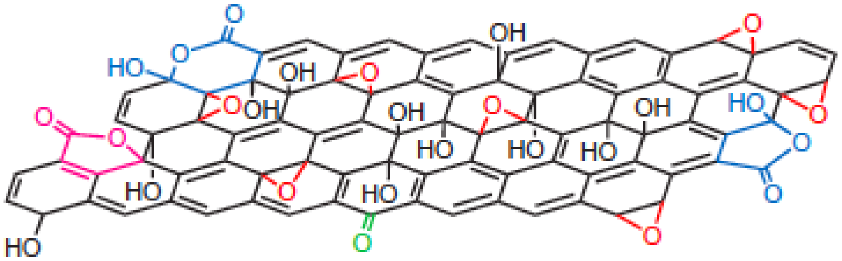

Figure 1–7. Modified Lerf-Klinowski model of graphene oxide plane decorated with hydroxyl (black), epoxide (red), ketone(green), lactol (blue), and ester (purple) [1.29].

In earlier studies by Klinowski's group, it was observed that graphite oxide layers consist of randomly distributed aromatic carbon rings and oxidized rings. They have discovered that hydroxyl and epoxide groups are heavily decorating the graphitic plane with C–OH and carboxylic acid groups attached on the edges of the plane. In addition, the study proposed that hydroxyl and epoxide groups are closely together on the plane from formation of phenol during deoxygenation reaction. Cai *et al.* later confirmed this from actual reading of SSNMR spectra [1.28]. Further study performed by Gao *et al.* revealed the presence of five and six membered lactol rings, ester from tertiary alcohol, and ketone groups on graphite oxide layer in addition to hydroxyl and epoxide groups [1.29]. Each of these groups is color coded in Figure 1–7. Although, these oxygen–containing groups act as defects, which cannot be fully removed through reduction processes, they also give unique properties such as hydrophilicity [1.26] and anti-bacterial characteristics [1.32]. Moreover, the defects react as centers for further attachment of functionalities [1.33].

To enable numerous solution processing techniques of chemically derived graphene, producing stable suspensions of single layer GO sheets is a key requirement. Ruoff *et al.* successfully demonstrated dispersion of chemically derived graphene in polar aprotic solvents like DMF, NMP, and dimethyl sulfoxide (DMSO) [1.33]. Functionalization of GO sheets by isocyanates resulted in less hydrophilic product. They observed that the functionalized GO layers do not disperse well in polar protic solvents including methanol and ethanol. Further effort in dispersing colloidal suspension of exfoliated GO sheets reduced by hydrazine hydrate failed by aggregation [1.26]. From the demonstrated results, early studies concluded that hydrophilicity of GO is primary contributor in stabilizing the suspension. Later on, Li *et al.* discovered that the electrostatic force of colloidal GO sheets is a key attribute in forming stable suspension rather than hydrophilic characteristic of GO [1.18]. Electrostatic force originates from negative surface charges from ionization of carboxylic acid and phenolic hydroxyl groups. They underlined the importance of removing residual metal salts and acids on the GO surfaces from the oxidation process. Residual electrolytes tend to de-stabilize and neutralize surface charges. From the results, the carboxylic acid groups remained even after chemical reduction in hydrazine maintaining negatively charges on the surface. Zeta potential measurements of reduced GO dispersion with respect to solution pH have revealed that ionization level of carboxyl acid groups is chemically controllable. The hydrophilic nature and electrostatic force from the negative charges produce stable suspension of single layer GO in aqueous media. These advantages have made processing large quantity of graphene–based materials via simple solution processing techniques.

1.2 Electrophoretic Deposition (EPD)

1.2.1 Fundamentals and background

Electrophoretic deposition (EPD) is a promising technique for GO deposition with a number of advantages including simple experimental apparatus, economic cost, high throughput, fine control of film thicknesses, scalability and broad selection of substrates [1.34]. EPD is a two-step process: (1) electrophoresis of charged colloidal particles followed by (2) deposition [1.35]. Surface charges on colloidal particles are important in achieving stable colloidal suspensions. Four different charge developing mechanisms on particles exist; (1) dissociation or ionization of surface groups (eg. adsorption of carboxylic acid), (2) re-adsorption of potential-determining ions (eg. H^+/OH^-), (3) adsorption of ionized surfactants, and (4) isomorphic substitution [1.35]. Surface charges attract counter ions around the particle forming an electric double layer. Figure 1–8 is a diagram of a charged particle in solution with a potential plot. Upon applied electric field, the charged particle and adsorbed counter ions move in opposite directions. However, fraction of the counter ions close to the particle surface move along with the particle due to strong attraction, creating shear in the electric double layer. Zeta potential denoted as ζ is the potential difference between the particle and the surface of shear. High zeta potential refers to thicker electric double layer and higher electrostatic force to overcome Van der Waals attraction between particles, thus creating more stable dispersion. Another important parameter in making stable dispersion is the dielectric constant of the liquid solution. Dielectric constant is related to the ability to conduct electricity [1.36]. Low dielectric constant gives insufficient dissociative power to create ions in solution. Liquids with high dielectric constant produce excess ions and lower the electric double layer thickness, resulting in aggregation. Experimental study by Powers has shown that dielectric constant between 12 and 25 is required for EPD [1.37]. During electrophoresis, interaction between the surface charge and electric field is the only acceleration force acting on the particle. Other forces from viscous drag, counter ions, and distortion of double layer slow down the particle movement.

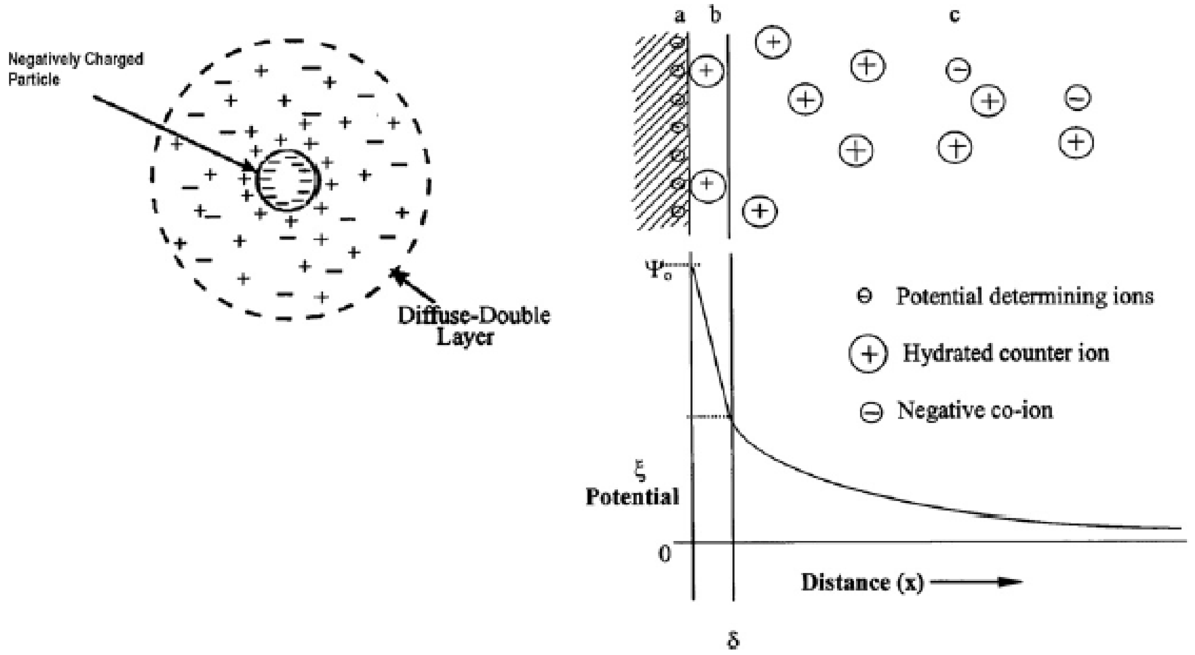

Figure 1–8. Schematic diagram of a charged particle and electric double layer (a) surface charge, (b) Stern layer, (c) diffuse layers of counter-ions [1.38].

1.2.2 Deposition kinetic models

The formation of deposit is primarily governed by suspension concentration, voltage, deposition time, and electrophoretic mobility of the particle. Thus, it is important to understand deposition kinetics in order to control the deposited amount. Hamaker has established a kinetic model for EPD [1.39].

$$m(t) = C\mu SEt \tag{1.1}$$

Equation 1.1 gives linear dependence of deposited mass (m) to deposition time (t). In addition, suspension characteristics including concentration (C), electrophoretic mobility of particles (μ), deposition area (S) and electric field strength (E) are related to the deposition kinetics. Hamaker model is only valid for a short period of time where there is no change in suspension characteristics. To take into account of concentration change during deposition, Sarkar and Nicholson developed kinetic models for constant-current and constant-voltage conditions using mass balance [1.35].

$$m(t) = M(1 - e^{-t/\tau})$$

$$\tau = \frac{M}{\mu I \rho C_o} \tag{1.2}$$

where m(t) is deposit mass with respect to time, M is initial mass of particles, τ is kinetic parameter, μ is electrophoretic mobility, I is applied current, ρ is density, and C_o is initial concentration. The model assumes no decrease in particle concentration from any process other than EPD. In a constant–voltage condition, the deposition rate decreased with increasing deposition time. The insulating character of the deposit increases the electrical resistance of the cell. As a result, the potential inducing electrophoresis decreases and slows down particle motion. Deposition is self–limiting because no deposit is possible when electric field gradient is negligible. In contrast, constant–current condition avoids problems from potential drop and limited deposition rate. Figure 1–9 displays relationship between deposited weight and time in four different conditions. The deposited weight is linearly dependent on time in the case of constant–current with constant–concentration, which reflects Hamaker's model. Ideally, if there is no change in the applied current or concentration, the deposited weight should linearly increase. However, this is only achieved for the first several minutes in real life conditions. In the other three conditions, linear dependency is valid for instantaneous time. In constant–voltage with varying–concentration condition, the relationship rapidly deviates from the linear initial behavior. Therefore, deposition kinetic model should be carefully picked considering EPD conditions especially at longer deposition time.

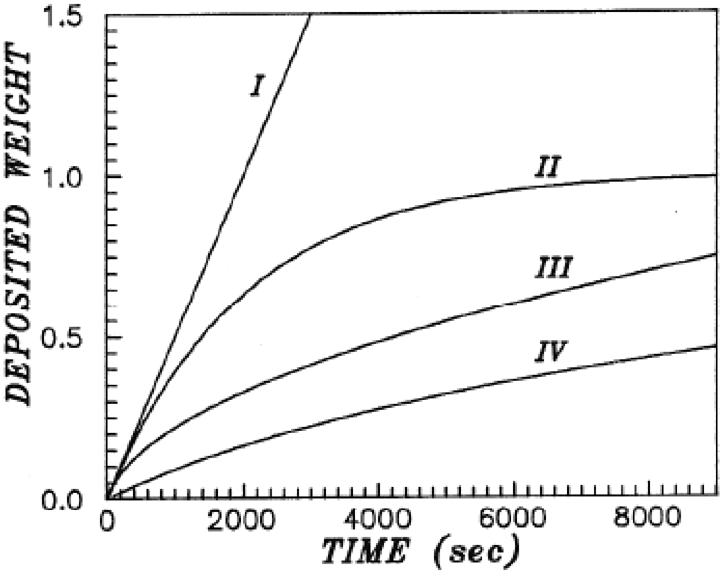

Figure 1–9. Schematic plot of deposited weight with respect to time – (I) constant current/constant concentration, (II) constant current/varying concentration, (III) constant voltage/constant concentration, (IV) constant voltage/varying concentration [1.35].

1.2.3 Previous studies on EPD of graphene-based materials

Graphene–based films have been electrophoretically deposited for applications including field emission devices [1.3], supercapacitors [1.27, 1.40], gas sensors [1.41], and antibacterial coatings [1.32]. In–depth review on applications of EPD of GO films by Chavez-Valdez *et al.* was recently preformed [1.34]. From previous studies, GO films were deposited on various substrates including stainless steel [1.42, 1.43], p-type Si [1.42], SiO_2 [1.44], nickel foam [1.40], indium tin oxide (ITO) coated glass [1.45], and Al [1.41]. Electrophoretic mobility of GO is negative and anodic EPD is performed for the most cases [1.42, 1.43]. EPD direction is reversible by attaching positively charged binders. Cathodic EPD of GO using Mg^{2+} binders have been demonstrated [1.3, 1.32, 1.40]. Attachment of Mg^{2+} promoted better adhesion of the films to the substrates [1.26].

In addition to the many advantage of EPD listed above, it has been proven to simultaneously reduce GO during the deposition process. Thus, EPD can potentially reduce or eliminate subsequent reduction process. Ishikawa and co-workers deposited GO on SiO_2/Si and conductive glass substrates to obtain transparent conductive films [1.44]. They obtained GO films with relatively lower oxygen content than the ones that were reduced by hydrazine. The GO films produced with EPD had C–C content of ~ 81 %. An *et al.* further confirmed the reduction process during EPD [1.42]. They compared oxygen contents of EPD GO films and GO paper from vacuum filtration. From Fourier Transform Infrared Spectroscopy (FT-IR) analysis, EPD GO has shown significant reduction in surface hydroxyl groups compared to the GO paper. From X-ray photoelectron spectroscopy (XPS) analysis, C/O atomic ratios of EPD–GO, GO Paper, and thermally annealed EPD–GO were 6:2:1, 1:2:1 and 9:3:1, respectively. These results have shown that EPD can remove oxygen–containing defects and deposited GO films can be further reduced via low temperature thermal annealing.

In order to fine control film deposition, understanding EPD kinetics for GO is important. Diba *et al*. performed quantitative evaluation of EPD kinetics of GO [1.45]. GO was deposited on ITO electrodes using low voltages to avoid current fluctuations caused by reduction at voltages above 10 V. The fluctuations could also result from evolution of gaseous by–products and water electrolysis. Figure 1–10 displays current density curves obtained during EPD. Current density curves at low voltages showed monotonic decrease with increasing deposition time due to the insulating nature of GO. The observed reduction is expected for constant voltage EPD and reflects well-controlled deposition process [1.35]. Measured deposit weight after heat treatment was converted into film thickness assuming density of 2.09 g/cm^3 from a previous study [1.46]. The converted film thicknesses displayed a good agreement with prediction from the Hamaker's model. Converted film thicknesses of non-heat treated samples have shown almost linear dependence to deposition time but deviated from the prediction. They explained this from the mass loss during heat-treatment by removal of water and contribution of wrinkles to uneven film thickness.

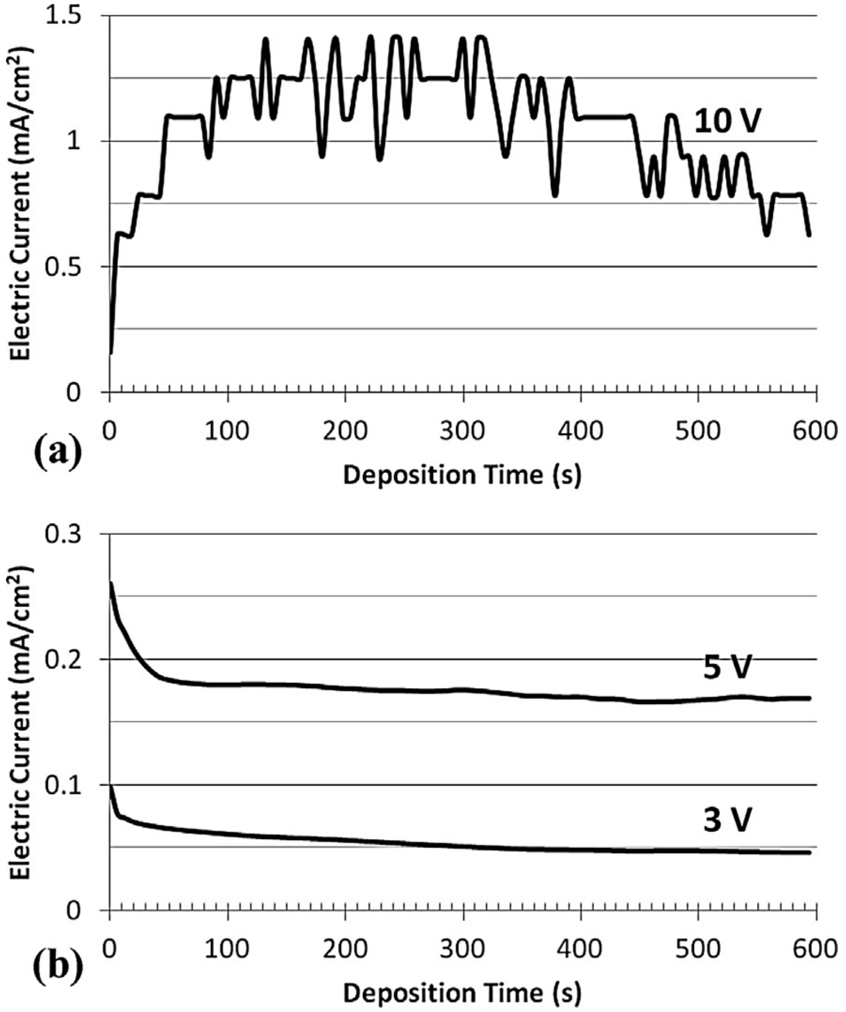

Figure 1–10. Current density curve during EPD at (a) high voltage and (b) low voltages [1.45].

Microstructure affects material properties such as wetting, electrical, and mechanical. Random orientation of GO layers and wrinkling of deposited films are commonly observed in EPD GO [1.3, 1.27, 1.32, 1.40, 1.41, 1.43, 1.45]. The wrinkles originate from distortion of carbon atom plane due to hydroxyl defects and overlapping of monolayer GO [1.31, 1.45]. Cathodic EPD using Mg^{2+} binder has produced almost perpendicularly oriented GO sheets with sharp edges [1.3, 1.32]. Subsequent heat treatment can help producing smoother surface. From tapping mode atomic force microscopy (AFM) study by Diba *et al*., average surface roughness values of deposited GO films before and after heat treatment were 28.57 nm and 4.51 nm, respectively [1.45]. In contrast, chemical reduction processes using hydrazine [1.32, 1.40] and sodium borohydride [1.27] has not shown significant change in film microstructures. Hasan *et al.* studied the effect of suspension pH to GO film deposition and microstructure [1.43]. Figure 1–11 shows photographs and SEM micrographs of films deposited in two different solutions.

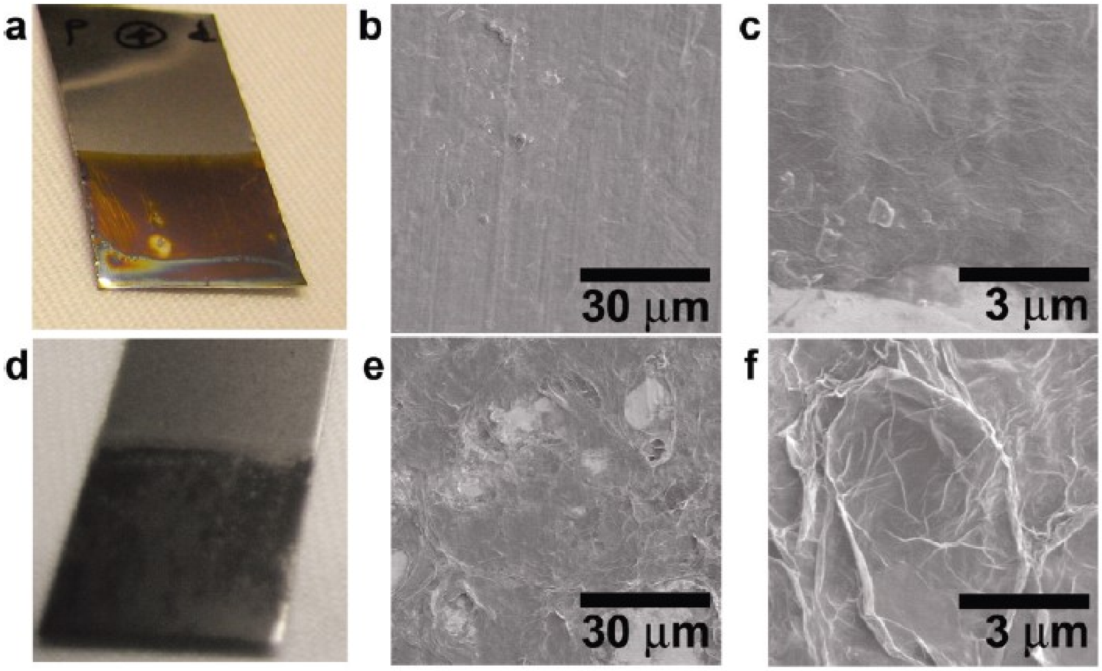

Figure 1–11. Photograph (a) and SEM micrographs (b,c) of films deposited in basic solution (pH 11.5) and photograph (d) and SEM micrographs (e,f) of films deposited in acidic solution (pH 2.8) [1.43].

GO suspension at pH 11.5 produced flat films with occasional wrinkles on the anode. Films from acidic solution at pH 2.8 produced porous microstructure consisting of stacked domains of bundled GO. In addition, colloidal GO sheets were primarily deposited on the cathode in acidic solution with few spotted deposits on the anode. This is due to a sharp reduction in zeta potential below pH 4 causing agglomeration of the suspended colloidal graphene. Moreover, the black color of the deposit shown in Figure 1–11(d) indicates that acidic solution has partially reduced the GO films. Previous studies on EPD GO were mostly focused on its applications, microstructures, and kinetics. Adhesions between the films and substrates were only described in qualitative measurements [1.45]. Therefore, further study is needed in EPD of GO films and the interaction with substrate materials to optimize electron transport and coating lifetime.

1.3 Mechanical Properties of GO

1.3.1 Quasi-static mechanical testing

Understanding the mechanical properties of materials is essential for optimizing device lifetime. Pristine graphene monolayer has shown a superior mechanical strength with in–plane Young's modulus of 1.0 ± 0.1 TPa and intrinsic strength of 130 ± 10 GPa at strain of 0.25 [1.7]. Emergence of chemical derivation using GO as a precursor of new efficient ways to produce graphene–based materials has instated needs of further understanding of mechanical properties of GO. Theoretical evaluation by Paci *et al.* has revealed that defects from oxidation reduce the material strength by approximately 16 % [1.47]. The weakening is due to sp^2 carbon transition into sp^3 carbon upon oxidation. The defects did not cause break up of material and the fracture strength was still in the same order as pristine graphene. Experimental studies performed by various research groups confirmed weakening of single layer graphene upon oxidation [1.48-1.51]. Gomez–Navaro and co-workers measured Young's modulus using AFM nanoindentation of monolayer reduced GO. GO was produced using modified Hummers method and reduced using hydrogen plasma treatment. No information on the chemistry of the produced monolayer was given. From AFM nanoindentation technique, Young's modulus of the monolayer reduced GO was measure to be 0.25 ± 0.15 TPa, which is significantly lower than that of pristine graphene. In addition, stacked monolayer of three or more layers exhibited an order of magnitude lower value of Young's modulus. Similar reduction in mechanical properties was observed with bundling of single–walled CNTs [1.49, 1.52, 1.53]. From Robinson *et al.*, Young's modulus of 4 nm and 20 nm films of GO sheets reduced by thermal annealing in hydrazine vapor were measured to be 185 GPa. However, it is hard to compare these values with other experimental data due to the absence of quantification of oxygen-bearing species after reduction process. Suk *et al*. performed the first study in elastic properties of GO using AFM nanoindentaion. Produced GO platelets by modified Hummers method did not undergo further reduction process and had C/O atomic ratio of 5:1. The platelets were drop-casted onto holey carbon films to obtain suspended freestanding GO monolayer. To avoid AFM tip instabilities during the measurements due to cantilever jumping and snapping, they scanned across the suspended film using contact mode instead of single point indentation. Effective Young's modulus was measured to be 207.6 ± 23.4 GPa, which is similar to Young' modulus of reduced GO films from previous studies [1.49, 1.50]. Kang *et al*. employed nanoindentation with dynamic contact module (DCM) system to obtain more precise and accurate measurements [1.48]. DCM provides vertical displacement resolution of 0.0002 nm and load resolution of 1 nN [1.48]. GO films were deposited using EPD technique on ITO glass substrates followed by etching of the substrate to release and suspend the deposited film on a Cu grid. Measured modulus was around three times higher than previous AFM nanoindentation measurements. Young's modulus ranged from 695 ± 53 GPa to 697 ± 15 GPa with ultimate tensile strength from 3 to 33 GPa. Ranjbartoreh *et al*. performed uniaxial tensile, microindentation, and bending test on graphene paper [1.54]. Graphene papers were produced by vacuum filtration of GO synthesized using modified Hummers method. No quantitative information on the oxygenated defects present in the graphene paper was provided. Ultimate tensile strength and elastic modulus of 3 μm thick papers were 78 MPa and 32 GPa at ultimate strain of 0.0040, respectively. These values were much lower than previously reported values. However, extremely high bending modulus of elasticity at 2.7 TPa was observed. They compared indentation testing results of specimens before and after heat treatment at 400 °C under argon for 5 hrs. Non-heat treated graphene papers obtained hardness and compressive elastic modulus of 3.92 kgf/mm^2 and 2.66 GPa, respectively. Heat-treated graphene papers achieved significant increase in hardness and the modulus at 217.53 kgf/mm^2 and 17.04 GPa, respectively. From these observations, it is clear that film thickness and amount of oxygenated defects affect the mechanical properties of chemically derived graphene. Mechanical properties of GO should be carefully compared between studies with different experimental procedures due to this discrepancy.

1.3.2 Dynamic mechanical testing

Previous mechanical characterization of graphene-based materials has been done mostly in quasi-static condition. However, materials are more likely to undergo deformation in dynamic condition during manufacturing processes and operation. Recently, Lee and co-workers performed dynamic mechanical testing using laser induced projectile impact test (LIPIT) on free-standing multilayer graphene [1.55]. They suspended mechanically exfoliated multilayer graphene films with thickness ranging from 10 nm to 100 nm onto a grid sample holder. Dynamic mechanical tests using silica micro-bullets revealed specific penetration energy of multilayer graphene to be ~ 10 times higher than macroscopic steel sheet. Further study in dynamic mechanical behavior of GO is needed for a better understanding of its mechanical response in real-life device applications.

1.4 Dynamic Mechanical Testing using Nano-impact

1.4.1 Nano-impact device set-up

Recent development of high-strain rate nano-impact testing technique developed by Beake *et al.* has enabled dynamic mechanical property assessment of materials at micro- and nano- scale with single and repeated localized impacts [1.56]. Figure 1–12 shows a schematic diagram of the nano-impact testing device. The device is pendulum-based and high-strain rate impacts are applied by diamond headed indenter tip fixed on the pendulum. Pendulum movement is done around frictionless pivot and the internal friction of the machine is assumed to be minimal. Electromagnetic coil located at the top part of the device is responsible for applying constant load during impact tests. Loading is achieved by flowing constant current through the electromagnetic coil. The capacitive transducer located behind the indenter tip detects the pendulum displacement. For a localized impact, magnetic field imposed by the solenoid fixed at the bottom of pendulum holds the indenter tip away from the specimen surface. When a constant current is established through the loading coil, solenoid current is switched off to release the indenter tip and make a single impact on the surface. This type of impact test provides impact velocities in mm/s scale and strain rate of ~ 10^4 s^{-1}.

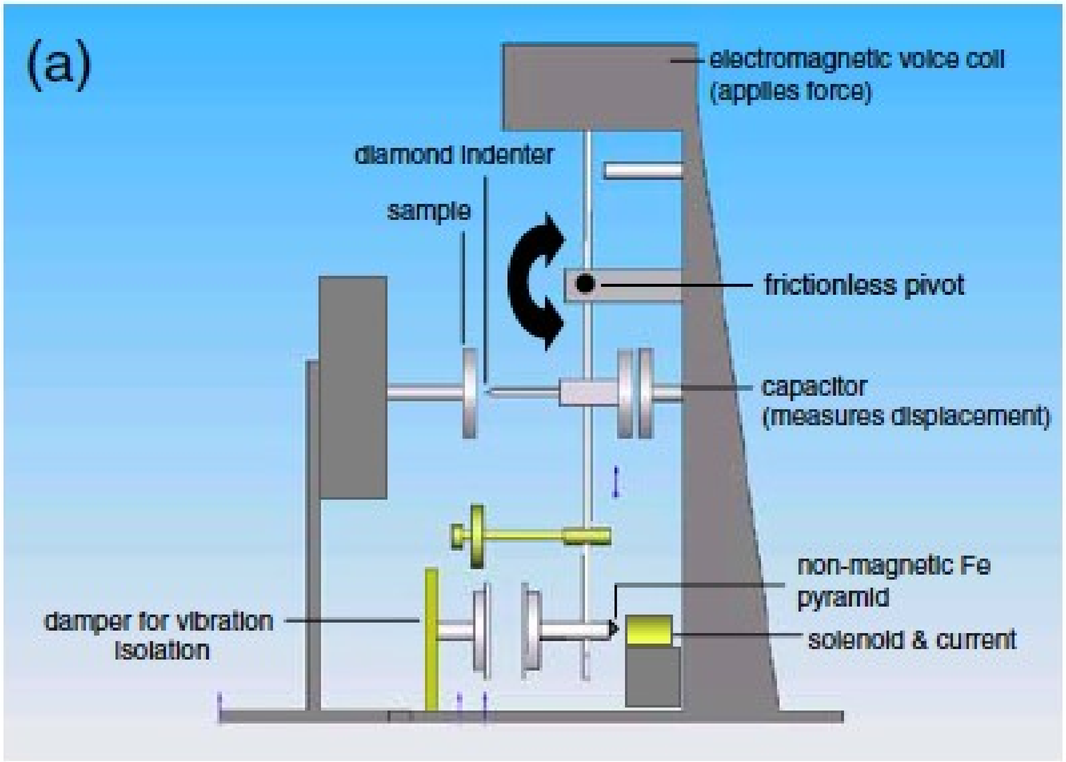

Figure 1–12. Schematic diagram of nano-impact device set-up [1.57].

1.4.2 Previous studies on coatings

A wide range of coating materials has been tested; amorphous carbon [1.56, 1.58], CrAlTiN [1.56], diamond like carbon (DLC) [1.59], TiAlN [1.60], AlCrN [1.60], multilayer coatings of TiCN and Al_2O_3 [1.61, 1.62], TiFeN [1.63], and TiFeMoN [1.63]. Repeated localized impact tests were performed on these coating to observe fracture behavior with respect to applied load and number of cycles. Beake assessed impact wear of DLC coatings using the time at first fracture and probability of fracture within a given time [1.59]. Fracture was defined as an abrupt change in depth corresponding to material displacement. Figure 1–13 displays a typical result from multiple impact test of a fractured coating [1.58].

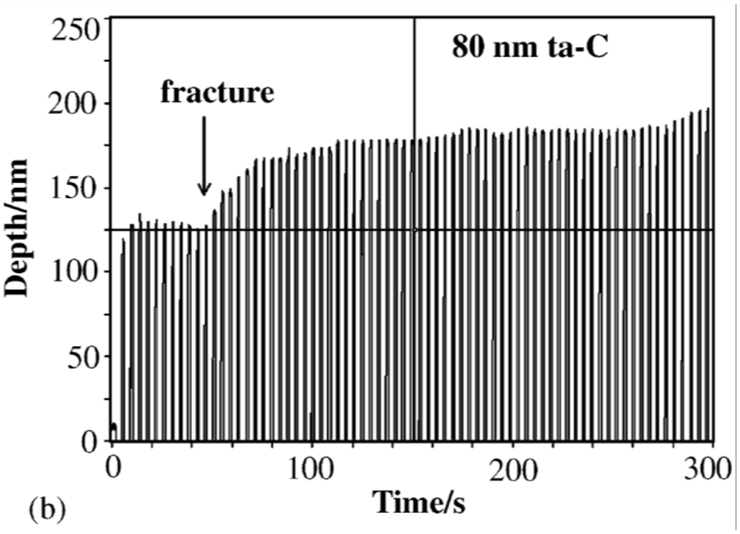

Figure 1–13. Depth vs. time plot from a multiple impact test [1.58].

A sudden jump in displacement vs. time curve indicates fracture. In another studies by Beake and co-workers, correlation between multiple impulse test results and H/E_r (hardness to reduced modulus ratio) from quasi-static tests was made [1.62]. Typically, H/E_r displays wear behavior of cutting tools and related to material resistance to plastic deformation. Coatings with lower H/E_r ratio had improved resistance to fracture. Jennett *et al*. developed fast data acquisition technique for dynamic impact testing [1.64]. The new technique enabled instantaneous measurements of position, velocity, acceleration, force, kinetic energy and potential energy during the tests. In addition, internal energy loss and effect of pendulum stiffening on data acquisition were observed to minimize error in the obtained results. Faisal *et al.* studied the influence of the indenter tip geometry on the film failure [1.65]. Two different film failure mechanisms were observed; (1) forward depth deviation and (2) backward depth deviation. Figure 1–14 illustrates the two mechanisms. Forward depth deviation (FDD) corresponds to an increase in contact depth with increasing number of cycles and observed in multiple impact tests with sharp Berkovich indenter tip. Backward depth deviation (BDD) is the reduction of the contact depth with increasing number of cycles due to swelling of the delaminated film. BDD of film was observed with spherical indenter tips. Both types of film failure were observed in a previous study [1.66]. Assessment in early studies was mostly made from measuring final impact depth and monitoring increase in probe depth caused by fracture. These types of analysis are rather qualitative and fail to quantify energy causing failure. In order to better analyze mechanical properties in dynamic deformation condition, a development of model to quantify the energy of impact is needed.

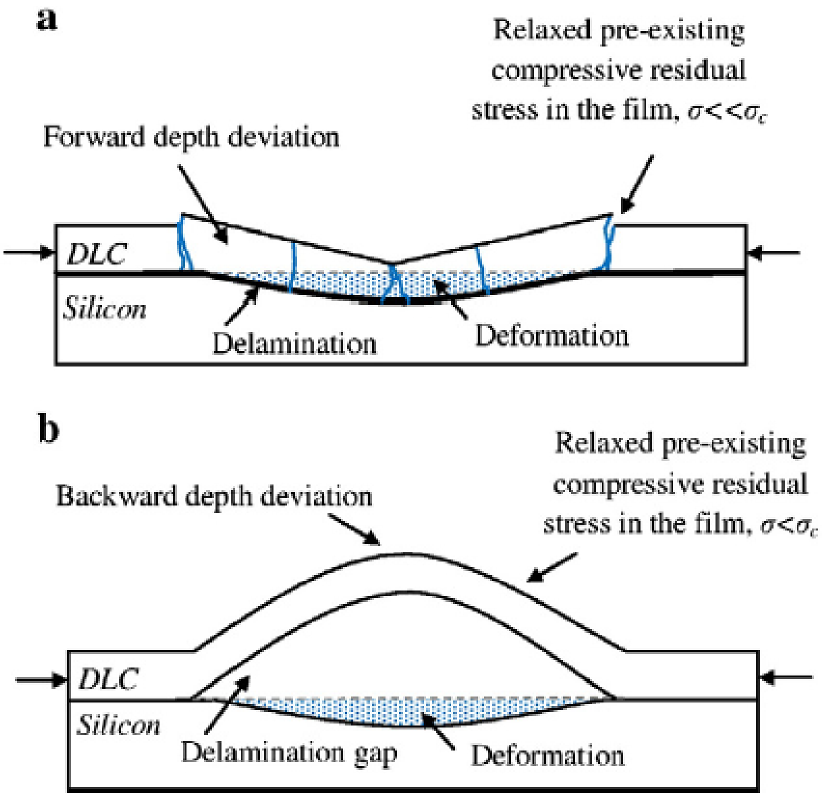

Figure 1–14. Schematic diagrams of film failure mechanisms – (a) forward depth deviation and (b) backward depth deviation [1.65].

1.4.3 Development of quantitative models

Constantinides and co-workers have developed an impact model using displacement response to extract useful material properties related to the impact deformation and extent of energy absorption [1.67]. Figure 1–15 is a typical displacement and velocity curves with respect to time. During an impact experiment, the velocity of the pendulum continuously rises until it hits the specimen surface. After the contact, the velocity sharply decreases due to the resistance of the material until it hits the maximum impact depth at minimum velocity. The material then undergoes elastic recovery and gives off recovered energy back to the pendulum. The pendulum rebounds from recovered elastic energy and oscillates until it loses energy completely.

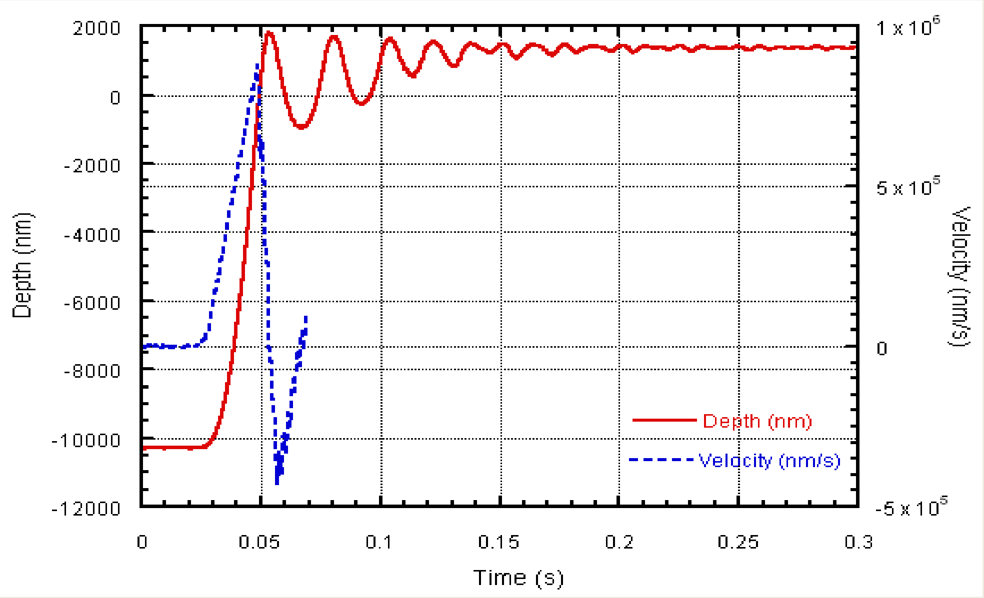

Figure 1–15. Typical depth and velocity response from single impact tests.

For quantitative analysis, displacement response from the point at maximum velocity to the rebound velocity is considered. Equations to extract material parameters including material specific impact resistance ratio (C), coefficient of restitution (e), and dynamic hardness (H_d) were derived. The developed mathematical model also enabled direct access to the hardness to modulus ratio (H/E) at a specific impact velocity. Given a condition where the residual depth is more accurately measured than the time of impact and recovery, we can evaluate impact resistance ratio C directly from the following equation by Andrews *et al.* [1.68],

$$\frac{x_r}{x_{\max}} = 1 - C \tag{1.3}$$

where x_r is measured residual depth and x_{max} is maximum depth of penetration. From previous study on elastoplastic work of sharp indenter, the following relationship between C and normalize plastic work is established [1.69],

$$C = d^* \frac{H}{E} = 1 - \frac{W_p}{W_t} \tag{1.4}$$

where W_p is plastic work, W_t is total work, and d* is indenter geometry constant. It can also extract H/E ratio directly from measurements. Coefficient of restitution is obtained from equation (1.5),

$$e = \left| \frac{v_{out}}{v_{in}} \right| = \left(\frac{3C}{2} \right)^{1/2} \tag{1.5}$$

where v_{out} is rebound velocity and v_{in} is impact velocity. From the derivations, the relationship between coefficient restitution and specific impact resistance ratio is established. Dynamic hardness is calculated as per equation (1.6),

$$H_d = \frac{3(v_{in} - v_{out})^2}{2\alpha x_r^3} \tag{1.6}$$

where m is mass of pendulum and α is indenter geometry parameter. Measured impact response of Al 1100 displayed good correlation with developed model, with calculated dynamic hardness closely matching with quasi-static hardness. However, impact behavior of annealed and work-hardened Au reflected rate-dependent energy absorption and calculated dynamic hardness of both materials were higher than their quasi-static hardness. The above model employs constant C and does not take account of rate-dependent material properties and strain-sensitivity of material.

1.5 Research Objectives

Objective of the project is to understand interfacial chemical properties and high-strain rate impact response of EPD GO films on Al alloy substrates. Adhesion between film and substrate is critical to ensure good device performance. Commercially available Al 1100, Al 5052, and Al 6061 plates were selected as substrates of interest due to their broad spectrum of applications and desirable properties including lightweight, good electrical and thermal conductivity, and corrosion resistance [1.70]. In addition, previous study has demonstrated reduction of GO films on Al substrates using chemical reaction of Al with HCl to produce H^+ for reduction reaction [1.71]. Thus, it would be interesting to observe chemical properties of GO films deposited on Al. This manuscript-based thesis contains two prepared manuscripts in chapters. The following contents are discussed in each chapter:

- Chapter 3 discusses general EPD characteristics and change in microstructures of EPD GO films with respect to applied potential and deposition time. In addition, it explores on adhesion of GO films on the three substrates from qualitative adhesion tests.
- Chapter 4 contains manuscript titled "*Understanding interfacial development of electrophoretically deposited graphene oxide films on Al alloys*." Elemental and chemical analyses of EPD GO films on Al 1100 and Al 5052 are performed using FT-IR and XPS depth profiling. Metal ion penetration into GO films is suggested from obtained results. Further, it explores change in chemical properties after low temperature heat treatment at 150 °C from high-resolution XPS spectra.
- Chapter 5 encloses manuscript on "*Dynamic mechanical characterization of electrophoretically deposited graphene oxide films on Al 5052 substrates*." Impact response of specimens with film thickness ranging from ~ 600 to 1700 nm were observed using Nano-impact testing technique. Tests are performed at seven different impact velocities. Coefficient of elastic restitution, dynamic hardness, and dynamic impact energy dissipation are quantified.

1.6 References

1.1. Chua, C.K. and M. Pumera, *Chemical reduction of graphene oxide: a synthetic chemistry viewpoint.* Chemical Society Reviews, 2014. **43**(1): p. 291-312.

1.2. Geim, A.K. and K.S. Novoselov, *The rise of graphene.* Nature Materials, 2007. **6**(3): p. 183-191.

1.3. Wu, Z.S., et al., *Field Emission of Single-Layer Graphene Films Prepared by Electrophoretic Deposition.* Advanced Materials, 2009. **21**(17): p. 1756-+.

1.4. Novoselov, K.S., et al., *Two-dimensional gas of massless Dirac fermions in graphene.* Nature, 2005. **438**(7065): p. 197-200.

1.5. Novoselov, K.S., et al., *Electric field effect in atomically thin carbon films.* Science, 2004. **306**(5696): p. 666-669.

1.6. Balandin, A.A., et al., *Superior thermal conductivity of single-layer graphene.* Nano Letters, 2008. **8**(3): p. 902-907.

1.7. Lee, C., et al., *Measurement of the elastic properties and intrinsic strength of monolayer graphene.* Science, 2008. **321**(5887): p. 385-388.

1.8. Liu, L., et al., *Graphene oxidation: Thickness-dependent etching and strong chemical doping.* Nano Letters, 2008. **8**(7): p. 1965-1970.

1.9. Cho, B., et al., *Graphene-based gas sensor: metal decoration effect and application to a flexible device.* Journal of Materials Chemistry C, 2014. **2**(27): p. 5280-5285.

1.10. Kim, K.S., et al., *Large-scale pattern growth of graphene films for stretchable transparent electrodes.* Nature, 2009. **457**(7230): p. 706-710.

1.11. Krishnamoorthy, K., A. Ramadoss, and S.J. Kim, *Graphene Oxide Nanosheets for Corrosion-Inhibiting Coating.* Science of Advanced Materials, 2013. **5**(4): p. 406-410.

1.12. Prasai, D., et al., *Graphene: Corrosion-Inhibiting Coating.* Acs Nano, 2012. **6**(2): p. 1102-1108.

1.13. Singh, V., et al., *Graphene based materials: Past, present and future.* Progress in Materials Science, 2011. **56**(8): p. 1178-1271.

1.14. Hernandez, Y., et al., *High-yield production of graphene by liquid-phase exfoliation of graphite.* Nature Nanotechnology, 2008. **3**(9): p. 563-568.

1.15. Lotya, M., et al., *Liquid Phase Production of Graphene by Exfoliation of Graphite in Surfactant/Water Solutions.* Journal of the American Chemical Society, 2009. **131**(10): p. 3611-3620.

1.16. Green, A.A. and M.C. Hersam, *Solution Phase Production of Graphene with Controlled Thickness via Density Differentiation.* Nano Letters, 2009. **9**(12): p. 4031-4036.

1.17. Li, X.L., et al., *Highly conducting graphene sheets and Langmuir-Blodgett films.* Nature Nanotechnology, 2008. **3**(9): p. 538-542.

1.18. Li, D., et al., *Processable aqueous dispersions of graphene nanosheets.* Nature Nanotechnology, 2008. **3**(2): p. 101-105.

1.19. Berger, C., et al., *Electronic confinement and coherence in patterned epitaxial graphene.* Science, 2006. **312**(5777): p. 1191-1196.

1.20. Somani, P.R., S.P. Somani, and M. Umeno, *Planer nano-graphenes from camphor by CVD.* Chemical Physics Letters, 2006. **430**(1-3): p. 56-59.

1.21. Li, X.S., et al., *Evolution of Graphene Growth on Ni and Cu by Carbon Isotope Labeling.* Nano Letters, 2009. **9**(12): p. 4268-4272.

1.22. Reina, A., et al., *Layer Area, Few-Layer Graphene Films on Arbitrary Substrates by Chemical Vapor Deposition.* Nano Letters, 2009. **9**(8): p. 3087-3087.

1.23. Yu, Q., et al., *Graphene segregated on Ni surfaces and transferred to insulators.* Applied Physics Letters, 2008. **93**(11): p. 113103.

1.24. Li, X.S., et al., *Large-Area Synthesis of High-Quality and Uniform Graphene Films on Copper Foils.* Science, 2009. **324**(5932): p. 1312-1314.

1.25. Hummers, W.S. and R.E. Offeman, *Preparation of Graphitic Oxide.* Journal of the American Chemical Society, 1958. **80**(6): p. 1339-1339.

1.26. Stankovich, S., et al., *Synthesis of graphene-based nanosheets via chemical reduction of exfoliated graphite oxide.* Carbon, 2007. **45**(7): p. 1558-1565.

1.27. Lake, J.R., et al., *Graphene metal oxide composite supercapacitor electrodes.* Journal of Vacuum Science & Technology B, 2012. **30**(3).

1.28. Cai, W.W., et al., *Synthesis and solid-state NMR structural characterization of (13)C-labeled graphite oxide.* Science, 2008. **321**(5897): p. 1815-1817.

1.29. Gao, W., et al., *New insights into the structure and reduction of graphite oxide.* Nature Chemistry, 2009. **1**(5): p. 403-408.

1.30. He, H.Y., et al., *A new structural model for graphite oxide.* Chemical Physics Letters, 1998. **287**(1-2): p. 53-56.

1.31. Lerf, A., et al., *Structure of graphite oxide revisited.* Journal of Physical Chemistry B, 1998. **102**(23): p. 4477-4482.

1.32. Akhavan, O. and E. Ghaderi, *Toxicity of Graphene and Graphene Oxide Nanowalls Against Bacteria.* Acs Nano, 2010. **4**(10): p. 5731-5736.

1.33. Stankovich, S., et al., *Synthesis and exfoliation of isocyanate-treated graphene oxide nanoplatelets.* Carbon, 2006. **44**(15): p. 3342-3347.

1.34. Chavez-Valdez, A., M.S.P. Shaffer, and A.R. Boccaccini, *Applications of Graphene Electrophoretic Deposition. A Review.* Journal of Physical Chemistry B, 2013. **117**(6): p. 1502-1515.

1.35. Sarkar, P. and P.S. Nicholson, *Electrophoretic deposition (EPD): Mechanisms, kinetics, and application to ceramics.* Journal of the American Ceramic Society, 1996. **79**(8): p. 1987-2002.

1.36. Van der Biest, O.O. and L.J. Vandeperre, *ELECTROPHORETIC DEPOSITION OF MATERIALS.* Annual Review of Materials Science, 1999. **29**(1): p. 327-352.

1.37. Powers, R.W., *Electrophoretic Forming of Beta-Alumina Ceramic.* Journal of the Electrochemical Society, 1975. **122**(4): p. 490-500.

1.38 Weise NL, editor. SME Mineral processing handbook, vol. 1. New York: Society of Mining Engineers;1985. p. 5.42.

1.39. Hamaker, H.C., *Formation of a deposit by electrophoresis.* Transactions of the Faraday Society, 1940. **35**(3): p. 0279-0286.

1.40. Xia, X.H., et al., *Graphene Sheet/Porous NiO Hybrid Film for Supercapacitor Applications.* Chemistry-a European Journal, 2011. **17**(39): p. 10898-10905.

1.41. Tang, L.H., et al., *Uniform and rich-wrinkled electrophoretic deposited graphene film: a robust electrochemical platform for TNT sensing.* Chemical Communications, 2010. **46**(32): p. 5882-5884.

1.42. An, S.J., et al., *Thin Film Fabrication and Simultaneous Anodic Reduction of Deposited Graphene Oxide Platelets by Electrophoretic Deposition.* Journal of Physical Chemistry Letters, 2010. **1**(8): p. 1259-1263.

1.43. Hasan, S.A., et al., *Transferable Graphene Oxide Films with Tunable Microstructures.* Acs Nano, 2010. **4**(12): p. 7367-7372.

1.44. Ishikawa, R., et al., *Electrophoretic deposition of high quality transparent conductive graphene films on insulating glass substrates.* Asia-Pacific Interdisciplinary Research Conference 2011 (Ap-Irc 2011), 2012. **352**.

1.45. Diba, M., et al., *Quantitative evaluation of electrophoretic deposition kinetics of graphene oxide.* Carbon, 2014. **67**: p. 656-661.

1.46. Park, S., et al., *Colloidal Suspensions of Highly Reduced Graphene Oxide in a Wide Variety of Organic Solvents.* Nano Letters, 2009. **9**(4): p. 1593-1597.

1.47. Paci, J.T., T. Belytschko, and G.C. Schatz, *Computational studies of the structure, behavior upon heating, and mechanical properties of graphite oxide.* Journal of Physical Chemistry C, 2007. **111**(49): p. 18099-18111.

1.48. Kang, S.H., et al., *Mechanical properties of free-standing graphene oxide.* Diamond and Related Materials, 2013. **38**: p. 73-78.

1.49. Gomez-Navarro, C., M. Burghard, and K. Kern, *Elastic properties of chemically derived single graphene sheets.* Nano Letters, 2008. **8**(7): p. 2045-2049.

1.50. Robinson, J.T., et al., *Wafer-scale Reduced Graphene Oxide Films for Nanomechanical Devices.* Nano Letters, 2008. **8**(10): p. 3441-3445.

1.51. Suk, J.W., et al., *Mechanical Properties of Monolayer Graphene Oxide.* Acs Nano, 2010. **4**(11): p. 6557-6564.

1.52. Kang, S.-H., T.-H. Fang, and Z.-H. Hong, *Electrical and mechanical properties of graphene oxide on flexible substrate.* Journal of Physics and Chemistry of Solids, 2013. **74**(12): p. 1783-1793.

1.53. Salvetat, J.P., et al., *Elastic and shear moduli of single-walled carbon nanotube ropes.* Physical Review Letters, 1999. **82**(5): p. 944-947.

1.54. Ranjbartoreh, A.R., et al., *Advanced mechanical properties of graphene paper.* Journal of Applied Physics, 2011. **109**(1).

1.55. Lee, J.H., et al., *Dynamic mechanical behavior of multilayer graphene via supersonic projectile penetration.* Science, 2014. **346**(6213): p. 1092-1096.

1.56. Beake, B.D. and J.F. Smith, *Nano-impact testing - An effective tool for assessing the resistance of advanced wear-resistant coatings to fatigue failure and delamination.* Surface and Coatings Technology, 2004. **188-189**(1-3 SPEC.ISS.): p. 594-598.

1.57. Constantinides, G., et al., *Quantitative Impact Testing of Energy Dissipation at Surfaces.* Experimental Mechanics, 2009. **49**(4): p. 511-522.

1.58. Beake, B.D., S.P. Lau, and J.F. Smith, *Evaluating the fracture properties and fatigue wear of tetrahedral amorphous carbon films on silicon by nano-impact testing.* Surface and Coatings Technology, 2004. **177-178**: p. 611-615.

1.59. Beake, B.D., *Evaluation of the fracture resistance of DLC coatings on tool steel under dynamic loading.* Surface and Coatings Technology, 2005. **198**(1-3 SPEC. ISS.): p. 90-93.

1.60. Beake, B.D., et al., *Coating optimisation for high speed machining with advanced nanomechanical test methods.* Surface and Coatings Technology, 2009. **203**(13): p. 1919-1925.

1.61. Beake, B.D. and N. Ranganathan, *An investigation of the nanoindentation and nano/micro-tribological behaviour of monolayer, bilayer and trilayer coatings on cemented carbide.* Materials Science and Engineering A, 2006. **423**(1-2): p. 46-51.

1.62. Beake, B.D., et al., *Investigating the correlation between nano-impact fracture resistance and hardness/modulus ratio from nanoindentation at 25-500 °C and the fracture resistance and lifetime of cutting tools with Ti1-xAlxN (x = 0.5 and 0.67) PVD coatings in milling operations.* Surface and Coatings Technology, 2007. **201**(8): p. 4585-4593.

1.63. Beake, B.D., V.M. Vishnyakov, and J.S. Colligon, *Nano-impact testing of TiFeN and TiFeMoN films for dynamic toughness evaluation.* Journal of Physics D: Applied Physics, 2011. **44**(8).

1.64. Jennett, N.M. and J. Nunn, *High resolution measurement of dynamic (nano) indentation impact energy: a step towards the determination of indentation fracture resistance.* Philosophical Magazine, 2011. **91**(7-9): p. 1200-1220.

1.65. Faisal, N.H., et al., *Influence of test methodology and probe geometry on nanoscale fatigue failure of diamond-like carbon film.* Surface and Coatings Technology, 2014. **242**: p. 42-53.

1.66. Wheeler, J.M. and A.G. Gunner, *Analysis of failure modes under nano-impact fatigue of coatings via high-speed sampling.* Surface and Coatings Technology, 2013. **232**: p. 264-268.

1.67. Constantinides, G., et al., *Quantifying deformation and energy dissipation of polymeric surfaces under localized impact.* Materials Science and Engineering a-Structural Materials Properties Microstructure and Processing, 2008. **489**(1-2): p. 403-412.

1.68. Andrews, E.W., et al., *Analysis of the impact of a sharp indenter.* International Journal of Solids and Structures, 2002. **39**(2): p. 281-295.

1.69. Giannakopoulos, A.E. and S. Suresh, *Determination of elastoplastic properties by instrumented sharp indentation.* Scripta Materialia, 1999. **40**(10): p. 1191-1198.

1.70. Davis, J.R., *Corrosion of aluminum and aluminum alloys*1999, Materials Park, OH: ASM International. vii, 313 p.

1.71. Domingues, S.H., et al., *Reduction of graphene oxide films on Al foil for hybrid transparent conductive film applications.* Carbon, 2013. **63**: p. 454-459.

1.72. Korsunsky, A.M., et al., *On the hardness of coated systems.* Surface & Coatings Technology, 1998. **99**(1-2): p. 171-183.

CHAPTER 2

Experimental Procedures

2.1 Graphene Oxide Synthesis

2.1.1 Starting material

All chemicals used in the synthesis were purchased from Sigma Aldrich, otherwise noted. GO sheets were synthesized using previously reported modified Hummers method [2.1] from expandable graphite (Grade 1721) provided from Asbury Carbon. Microwave-assisted thermal expansion technique was used. Upon 30 s of microwave, instant thermal decomposition of intercalated sulfuric acid (H_2SO_4) into SO_3 and H_2O vapor developed high pressure in between graphite layers causing expansion.

2.1.2 Synthesis of large-size graphene oxide

Two grams of the expanded graphite was slowly added to 200 mL of concentrated sulfuric acid (H_2SO_4) while mechanically stirring (Teflon impeller). Then, 15 g of potassium permanganate ($KMnO_4$) was added to the mixture followed by stirring for 2 hr at 35 °C. The mixture was moved to an ice bath to cool down temperature from exothermic reaction from added water in the following step. Graduated 500 mL of deionized water was added drop by drop for the first few minutes then larger amount slowly added as the amount of water in the mixture increased. Temperature of the mixture was monitored and maintained below 70 °C. The mixture was mechanically stirred for 1 hr followed by dilution in 3.0 L of deionized water. Then, 20 mL of hydrogen peroxide (H_2O_2, 30 wt. %) was slowly added to the diluted mixture and color of the mixture changed from dark brown to yellow. The mixture was set overnight to sediment synthesized GO sheets. The supernatant was decanted and the remaining solution was centrifuged at 3500 rpm for 15 min. Supernatant from the centrifugation was removed and remaining slurry was washed with 1 M HCl to remove manganese on the GO surface. The centrifugation and HCl wash were repeated 3 to 4 times to remove most of impurities present on the GO surface. Acid was removed by centrifugation at 12,000 rpm for 30 min and subsequent wash with deoinized water for 4 repeated times. The wash steps are very important for producing stable suspension of GO because remaining impurities and acids on the surface can de-stabilize surface charges and cause aggregation [2.2]. As-synthesized GO dispersion was a highly viscous paste. The paste was dried at 80 °C under vacuum for 24 h. Figure 2–1 shows SEM image of as-synthesized GO flakes ultrasonicated for an hour. The size of the GO sheets were approximately in a range of 5 to 10 µm and most of the sheets were comprised of single layer without overlapping. The C/O ratio of the as-synthesized GO flakes were 2.2 according to XPS measurements.

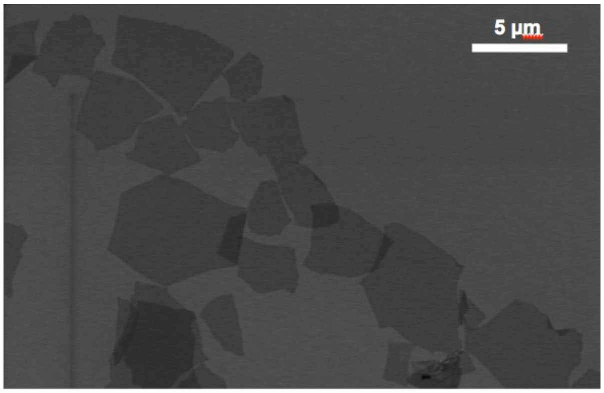

Figure 2–1. SEM image of as-synthesized GO flakes after 1 hr of ultrasonication.

2.2 Electrophoretic Deposition (EPD)

2.2.1 Starting material

Aluminum 1100, 5052, 6061 alloy plates were purchased through McMaster Carr. Elemental compositions of the Al alloy substrates provided from manufacturer are presented in Table 2–1.

Table 2–1. Elemental composition limits (max. %) of Al alloys – Al makes up the remaining composition (From the manufacturer data sheet).

Alloys	Si	Fe	Cu	Mn	Mg	Cr	Ni	Zn	Ti	Zr	Other

1100	1.0 (Si+Fe)		0.2	0.05	0.05	-	-	0.1	0.6	-	0.15
5052	0.25	0.7	0.1	0.1	2.8	0.35	-	0.2	-	-	0.15
6061	0.8	0.7	0.4	0.15	1.2	0.8	0.05	0.25	0.15	0.25	0.15

As-received Al 1100 plates had unpolished surface and as-received Al 5052 and Al 6061 alloy plates had mirror-finished surface. Thickness of the plates was ~ 1 mm. The plates were cut into 2 cm by 4 cm samples. All chemicals used in substrate preparation and electrophoretic deposition were purchased from Sigma Aldrich.

2.2.2 Preparation of substrate materials

The cut electrodes were cleaned by ultrasonication in acetone for 20 min followed by acetone and isopropyl alcohol (IPA) wash to remove impurities. Unpolished Al 1100 plates were chemically polished prior to flatten out the surface and remove existing native oxide layer. The chemical polishing procedures were adapted from a previous study by Alam *et al.* [2.3]. Al 1100 electrodes were dipped in a mixture of 85:15 phosphoric acid (H_3PO_4, 87 wt. %) and nitric acid (HNO_3, 70 wt. %) at 85 °C for 5 min followed by neutralization in 1 M sodium hydroxide (NaOH) for 5 min. The prepared Al 1100 substrates were washed with deionized water and stored in a desiccator.

2.2.3 EPD process

Synthesized GO paste was charged into pure ethanol followed by ultrasonication to make 2.0 mg/ml suspension. EPD was carried out in a parallel two-electrodes cell depicted in Figure 2–2. Negatively charged GO sheets make anodic deposition, therefore anodes were prepared from the Al alloy substrates. Al 1100 plate was used as cathodes for all samples. EPD was performed under constant-voltage condition. Approximately 50 mL of the suspension was used for each deposition process. No additional stirring was applied. Potential of 10 V, 15 V, and 20 V were applied for 5 min. At potential of 10 V, additional samples were deposited for 15 min and 30 min to observe the change in the film microstructure with respect to deposition time. The electrodes were drawn out from the suspension while the potential was still applied. The deposits were dried in air with applied potential to remove excess ethanol left on the surface followed by drying at room temperature in air for at least 1 hr. The dried samples were desiccated for 24 hrs to promote film adhesion on the substrates. Selected specimens were heat treated at temperatures of 150 °C in air for 1 hr.

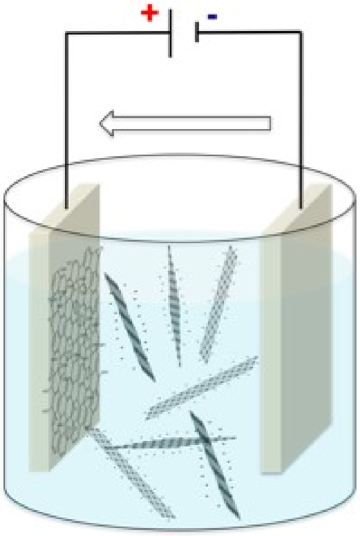

Figure 2–2. Schematic diagram of electrophoretic deposition cell.

2.3 Characterization of EPD Graphene Oxide Films

2.3.1 General characteristics

Electrophoretic mobility and zeta potential of the 2.0 mg/ml GO suspension in ethanol were measured with Dynamic Light Scattering (DLS, Malvern Zetasizer). Specimens were observed using optical microscopy and scanning electron microscopy (SEM, Hitachi S-4800 and S-3200) for their microstructure. Cross-sectional SEM micrographs were taken using 90° sample mounting stub. Average film thicknesses were calculated from cross-sectional micrographs using ImageJ software. At least ten different points were measured and averaged due to variance in film thickness within the deposited samples. The area covered by wrinkles was quantified using threshold and measurement function in ImageJ software. At least five different images taken at 1000 times magnification were averaged for each sample. Adhesion of as-deposited and heat-treated films on Al 1100, Al 5052, and Al 6061 was tested qualitatively with q-tip rub and scotch tape peel.

2.3.2 Elemental and chemical analyses

Fourier transform infrared spectroscopy (FT-IR, Thermo Scientific Nicolet 6700) was performed to observe the change in chemical structures of the films before and after heat treatment. Obtained FT-IR spectra were baseline corrected with poly-fit. Measurements were preformed at three different points within the same sample. X-ray photoelectron spectroscopy (Al Kα XPS, Thermos Scientific) was performed on films deposited on Al 1100 and Al 5052 substrates to obtain elemental compositions and chemical information. The X-ray source energy was 1486.6 eV with spot size of 400 μm. Elemental composition and C/O atomic ratio were averaged over XPS point analysis performed at three different points within the same sample. Depth profiling was employed to observe chemical structure change with respect to depth into the films. For each measured level, the GO films were etched with Ar ion with 3 keV for 200s. The etch rate depended on sample and heat-treated samples had relatively slow etch rate. The etching was continued until the film-substrate interface was reached. Obtained XPS spectra were peak fitted by using Avantage data system (Thermos Scientific) in Gaussian – Laurentzian peak shapes.

2.4 High–Strain Rate Mechanical Characterization

2.4.1 Nano-impact set-up

A schematic diagram of the Nano-impact device is presented in Figure 1–12 and detailed working principle of the device is explained in section 1.4.1. The device was enclosed to maintain a temperature of ~ 23 °C and isolated from external environment vibrations. A cube-corner indenter tip was used for the entire measurements.

2.4.2 Sample characteristics and test parameters

Only the films deposited on Al 5052 substrates at constant voltage of 10 V were used for nano-impact characterization. Samples had three different average film thicknesses, namely 662 ± 123 nm, 1320 ± 185 nm, and 1706 ± 178 nm with respect to increasing deposition time. Films were tested at 7 different impact loads. The loads and impact velocities at each of the applied loads are listed in Table 2–3. The applied velocities were within 2 % error. At least five different sample locations were tested at each load. Coefficient of restitution and dynamic hardness values are calculated from equations 1.5 and 1.6, respectively. SEM is used to observe deformation characteristics of the imprints after dynamic hardness tests.

Table 2–2. Applied load and corresponding impact velocities.

Load (mN)	V_{in} (mm/s)
0.1	0.288
0.5	0.337
1.0	0.392
2.5	0.512
5.0	0.669
7.5	0.796
10.0	0.896

2.5 References

2.1. Pham, V.H., et al., *Fast and simple fabrication of a large transparent chemically-converted graphene film by spray-coating.* Carbon, 2010. **48**(7): p. 1945-1951.

2.2. Li, D., et al., *Processable aqueous dispersions of graphene nanosheets.* Nature Nanotechnology, 2008. **3**(2): p. 101-105.

2.3. Alam, K.M., et al., *Fabrication of hexagonally ordered nanopores in anodic alumina: An alternative pretreatment.* Surface Science, 2011. **605**(3-4): p. 441-449.

2.4. Korsunsky, A.M., et al., *On the hardness of coated systems*. Surface & Coatings Technology, 1998. **99**(1-2): p. 171-183.

CHAPTER 3

General Results and Discussions

3.1 Preface

To start with EPD process, effect of deposition parameters on microstructure and adhesion of EPD GO films on Al Alloys is investigated. The present Chapter explores deposition on three different Al alloy substrates (Al 1100, Al 5052, and Al 6061), effects of applied potential and deposition time on film quality and thickness, low temperature heat treatment of deposited films, and adhesion between the films and substrates.

3.2 Deposition Characteristics

Measured electrophoretic mobility of the 2.0 mg/ml GO suspension in pure ethanol was -0.4498 ± 0.039 µm-cm/V-s. Figure 3–1 displays the obtained electrophoretic mobility plot from DLS reading. Negative mobility resulted in anodic deposition during EPD process.

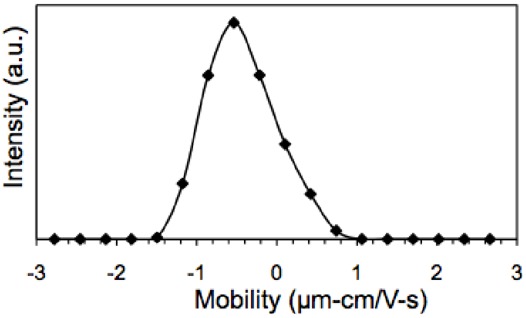

Figure 3–1. Electrophoretic mobility plot of 2.0 mg/ml GO suspension in pure ethanol.

Current density was continuously measured during deposition using a LabView program. Figure 3–2 (a) shows the obtained current density plots during deposition at three applied potentials. The parabolic decrease in current density is caused by increase in overall impedance and resistivity with respect to deposition time due to insulating nature of the GO deposit. The decrease is monotonic without significant fluctuation and presents well-controlled EPD process without severe water hydrolysis reaction or GO reduction. If the deposited GO is reduced during the deposition process, the current density would show significant fluctuation in the order of ± 0.5 mA/cm^2 of the initial current density with out a decrease as reported in previous studies [3.1, 3.2]. The current density increased almost linearly without voltage increase at all time frames as presented in Figure 3–2 (b). However, at a higher potential, the amount of current density drop with deposition time was greater. This is partly due to the increase in deposited coating resistivity with respect to the film thickness (i.e. applied potential). However, the overall resistivity change during the deposition process cannot be simply explained with the change in film resistivity, since there are other parameters affecting the resistance such as suspension resistivity and concentration.

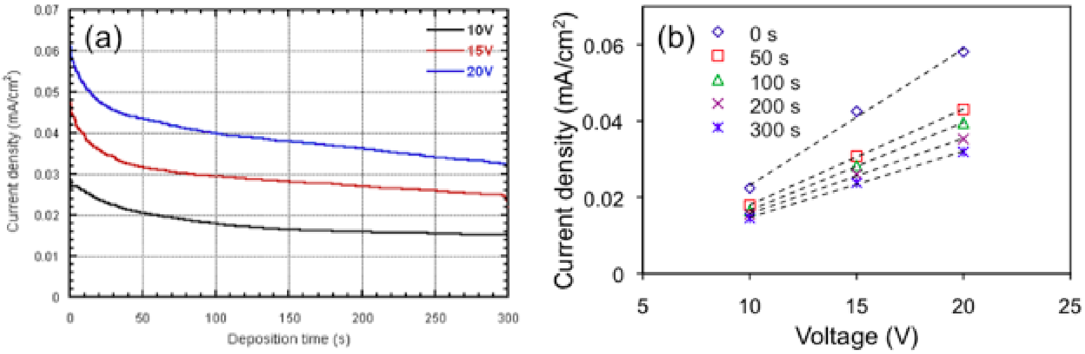

Figure 3–2. (a) Current density during deposition at 10 V, 15 V, and 20 V for 300 s and (b) current density vs. voltage plot at various deposition time.

Deposited films had light-brown color, which is common characteristic of GO and the color changed to black upon heat-treatment at 150 °C indicating reduction of the oxygenated defects. From XPS analysis, the carbon to oxygen (C/O) atomic ratio was 2.52 and 3.95 for as-deposited and thermally treated GO films respectively. Figure 3–3 (a) and (b) are photographs of as-deposited and heat-treated films respectively.

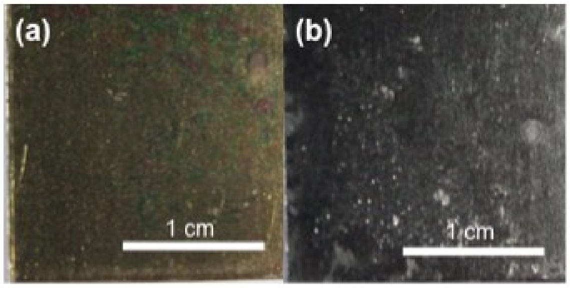

Figure 3–3. Photographs of GO deposited surfaces – (a) after EPD and (d) after heat treatment.

Averaged film thicknesses of specimens in relation with applied potential and deposition time is displayed in Figure 3–4 (a) and (b) respectively. Film thickness increased almost linearly with applied potential. We observed reduction in film thickness after heat-treatment due to removal of defects in between the layers resulting in a reduction of interlayer distance. Film thickness increased with deposition time as well, however, self-limiting behavior at long deposition time was observed. The plot presented in Figure 3–4 (b) correspond to constant-voltage model from Sarkar and Nicholson [3.3]. The maximum thickness is caused by the reduction in deposition rate with increasing deposition time during constant-voltage EPD. Electrophoretic mobility of the GO reduces as potential inducing electrophoresis decrease due to increased resistivity [3.3]. Deposition rate eventually reaches zero at very long deposition time when the electric field gradient becomes insufficient for electrophoresis of colloidal particles.

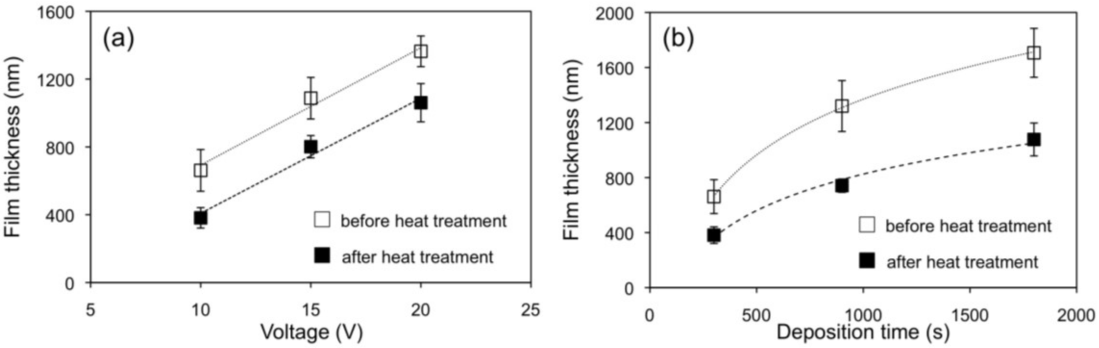

Figure 3–4. Film thickness measurements with respect to - (a) applied potential and (b) deposition time.

3.3 Microstructure Observations

Figures 3–5 and 3–6 display photographs and corresponding SEM micrographs of films deposited at three different deposition times and applied potentials, respectively. Increased in the air bubble coverage with increased deposition time is immediately noticeable from the photographs in Figure 3–5 (a), (c), and (e). The bubbles are formed primarily due to increase in O_2 evolution at the anode surface as the substrate is immersed for longer time. From SEM micrographs, the films consist of nearly flat stacks of GO with occasional wrinkles. Similar microstructure has been observed in previous studies on EPD GO [3.1, 3.4, 3.5]. The wrinkling is due to overlapping of the individual sheets as well as distortion of the tetrahedral carbon plane due to – OH defects on basal planes of sp^3 carbon [3.1, 3.6].

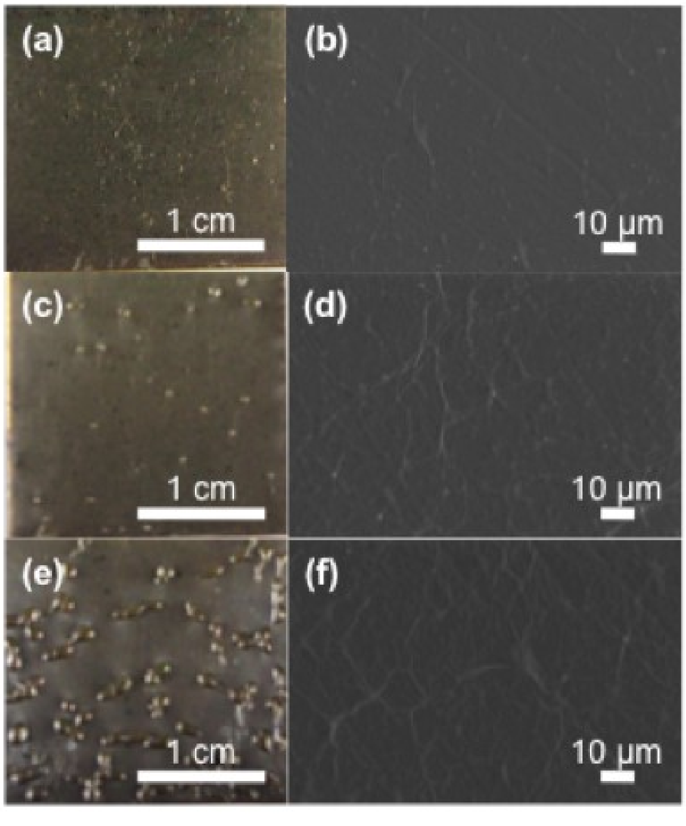

Figure 3–5. Photographs and corresponding SEM micrographs of specimens deposited at 10 V – (a,b) 5 min, (c,d) 15 min, (e,f) 30 min.

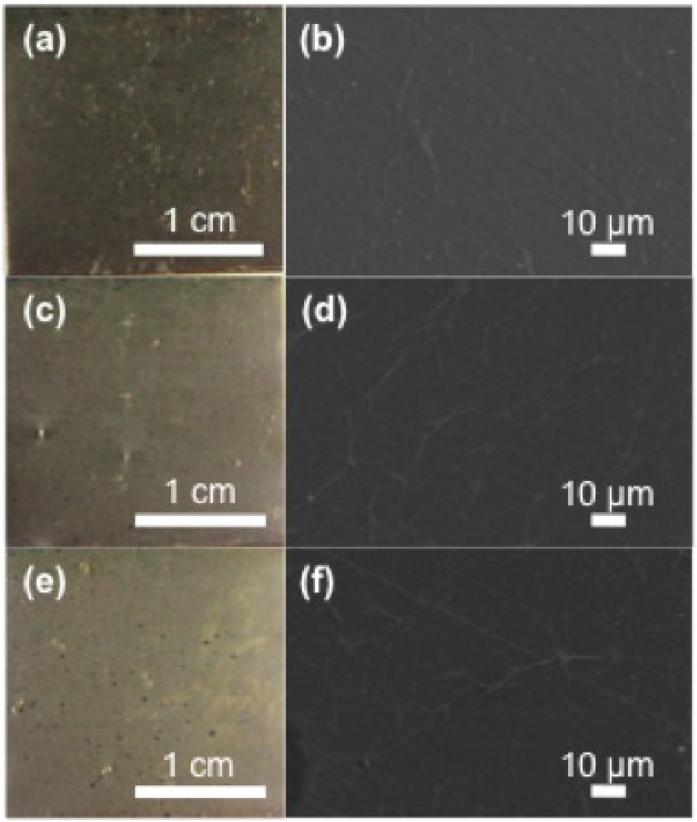

Figure 3–6. Photographs and corresponding SEM micrographs of films deposited for 5 min at (a,b) 10 V, (c,d) 15 V, (e,f) 20 V.

The fraction of surface covered by sporadic wrinkles increases with deposition time. From photographs presented in Figure 3–6, deposited films generally had no significant defects at all applied potentials. Few bubbles were present on the specimen surfaces deposited at 15 V and 20 V, however, the size of these bubbles were much smaller compared to the ones in Figure 3–5. Presence of micron-size bubbles was again confirmed from SEM micrograph for 20 V sample. Instead of continuous increase in wrinkles with potential, sudden increase of wrinkles at 20 V was observed. Films deposited at 10 V and 15 V had few sporadic wrinkles on the surface with no significant difference in microstructures of the two specimens. The main cause of severe wrinkling in films at high-applied potential is likely to be high deposition rate and aggregation of GO sheets at longer deposition time. The areas were averaged over at least five images taken at different points on the specimen surfaces. Figure 3–7 depicts plot relating the coverage area to deposition parameters. From the measurements, the change in the area covered by wrinkles at different applied potentials was statistically insignificant. However, dramatic increase in the area covered by wrinkles was observed with increase in deposition time. Therefore, the amount of wrinkles is largely affected by stacking of GO sheets rather than deposition rate. Wrinkles were relaxed after the heat treatment. The area covered by wrinkles was decreased to 50 % due to relaxation of distorted carbon plane upon removal of OH groups during the heat treatment.

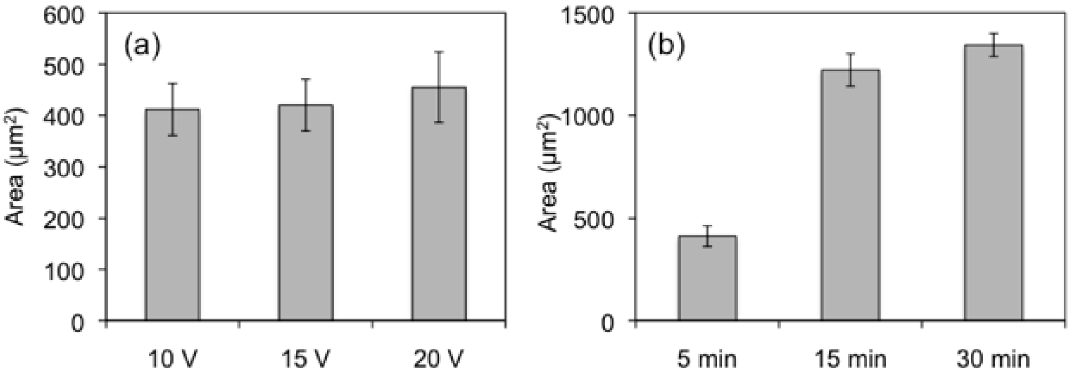

Figure 3–7. Measured area covered by wrinkles with respect to (a) voltage with 5 min deposition time and (b) deposition time at 10 V voltage.

From qualitative adhesion tests with q-tip rub and scotch tape peel, GO films deposited on Al 1100 and Al 5052 substrates displayed good adhesion. Films deposited Al 5052 substrates demonstrated stronger adhesion than films on Al 1100 substrates from scotch tape peel. Relatively high Mg content in Al 5052 may be the reason behind good binding to GO films. Mg content results in composite of MgO and Al_2O_3 in the native oxide layer. This is in line with previous study, where Mg^{2+} ions have been used as binders to promote better adhesion of GO films [3.7-3.9]. From these observations, it is likely that MgO promotes stronger adhesion with deposited films. However, the films deposited on Al 6061 substrates rub off easily after the deposition and upon heat treatment, the films cracked and peeled off completely from the substrate. This is not desirable for coating applications, however, it can be potentially used for producing freestanding films. Figure 3–7 displays film deposited on Al 6061 substrate after heat treatment. The detached films were as large as ~ 7 mm in size. The poor adhesion may be due to difference in composition and microstructure of native oxide layers present on Al 6061 substrates. For further studies of chemistry and mechanical properties, the films deposited on Al 6061 substrates were omitted.

Figure 3–8. Heat-treated GO film on Al 6061.

3.4 References

3.1. Diba, M., et al., *Quantitative evaluation of electrophoretic deposition kinetics of graphene oxide.* Carbon, 2014. **67**: p. 656-661.

3.2. An, S.J., et al., *Thin Film Fabrication and Simultaneous Anodic Reduction of Deposited Graphene Oxide Platelets by Electrophoretic Deposition.* Journal of Physical Chemistry Letters, 2010. **1**(8): p. 1259-1263.

3.3. Sarkar, P. and P.S. Nicholson, *Electrophoretic deposition (EPD): Mechanisms, kinetics, and application to ceramics.* Journal of the American Ceramic Society, 1996. **79**(8): p. 1987-2002.

3.4. Hasan, S.A., et al., *Transferable Graphene Oxide Films with Tunable Microstructures.* Acs Nano, 2010. **4**(12): p. 7367-7372.

3.5. Liu, X., et al., *Segregation Growth of Graphene on Cu-Ni Alloy for Precise Layer Control.* Journal of Physical Chemistry C, 2011. **115**(24): p. 11976-11982.

3.6. Lerf, A., et al., *Structure of graphite oxide revisited.* Journal of Physical Chemistry B, 1998. **102**(23): p. 4477-4482.

3.7. Wu, Z.S., et al., *Field Emission of Single-Layer Graphene Films Prepared by Electrophoretic Deposition.* Advanced Materials, 2009. **21**(17): p. 1756-+.

3.8. Akhavan, O. and E. Ghaderi, *Toxicity of Graphene and Graphene Oxide Nanowalls Against Bacteria.* Acs Nano, 2010. **4**(10): p. 5731-5736.

3.9. Xia, X.H., et al., *Graphene Sheet/Porous NiO Hybrid Film for Supercapacitor Applications.* Chemistry-a European Journal, 2011. **17**(39): p. 10898-10905.

CHAPTER 4

Understanding Interfacial Development of Electrophoretically Deposited Graphene Oxide Films on Al Alloys

Sumin Jin [1], Viet Hung Pham [2], James H. Dickerson [2,3], Mathieu Brochu [1]

[1] Department of Mining and Materials Engineering, McGill University, Montreal, QC
[2] Center for Functional Nanomaterials, Brookhaven National Laboratory, Upton, NY, USA
[3] Department of Physics, Brown University, Providence, RI, USA

4.1 Preface

Interfacial chemical properties are important in assessing adhesion between a film and a substrate. The following chapter investigates interfacial bonding chemistry of EPD GO films on Al 1100 and Al 5052 substrates using FT-IR and XPS with depth profiling. Films deposited on Al 6061 substrates were omitted in this study due to poor adhesion described in the previous chapter. Moreover, effect of heat treatment on microstructure of the deposited films is presented.

4.2 Abstract

Sustained adhesion between a film and its substrate is critical for electronic device and coating applications. Interfacial development between electrophoretically deposited graphene oxide films on Al 1100 and Al 5052 alloys were investigated using FT–IR and XPS depth profiling techniques. The results suggest metal ion permeation from the substrates into deposited graphene oxide films. The interface between the films and the substrates were primarily composed of Al–O–C bonds from oxygenated defects on graphene oxide plane rather than the expected formation of Al–C bonds. Films were heat treated at 150 °C and underwent a change in microstructure. Peak shifts in XPS spectra suggested changes in the chemical structure of the bonds between the films and the substrates.

4.3 Introduction

Electrophoretic deposition (EPD) is a promising technique for the deposition of carbonaceous nanomaterials, like graphene oxide (GO), given the number of advantages including simple experimental apparatus, economic cost, high throughput, fine control of film thicknesses, and broad selection of substrates [4.1, 4.2]. A recent review on GO EPD by Chavez-Valdez *et al.* summarized the potential applications of EPD GO, for example as electrochemical electrodes, field emission devices, sensors, and composite materials [4.1]. From previous studies, GO films were deposited on various substrates, including stainless steel [4.3, 4.4], p-type Si [4.4], SiO_2 [4.2], nickel foam [4.5], indium tin oxide (ITO) coated glass [4.6], and Al [4.4]. EPD has been proven to reduce oxygenated defects in GO during the deposition process. Ishikawa and co-workers deposited GO on SiO_2/Si and conductive glass substrates to obtain transparent conductive films [4.2]. Those GO films possessed a lower relative ratio of oxygen-containing groups than ones that were reduced by hydrazine. The GO films produced with EPD had C–C content of ~ 81 %. In addition, An *et al.* observed anodic reduction of GO during EPD process [4.4]. EPD GO films had C/O atomic ratio of 6.2:1. This was ~ 5 times higher than the measured ratio of 1.2:1 for GO paper produced by vacuum filtration. To deposit GO with fine control, Diva and co-workers performed quantitative evaluation of EPD kinetics of GO [4.6]. They used low voltages to avoid significant reduction of GO during the deposition processes. Experimental results displayed a good agreement with predictions from the Hamakers model [4.7]. Hasan *et al.* studied the effect of suspension pH to GO film deposition and microstructure [4.3]. Although many studies have been reported on GO EPD, no study has pointedly investigated the interfacial development between EPD GO films and their underlying substrates.

Maintenance of the adhesion between substrates and films is very important to ensure good device and coating performances with an extended coating lifetime. Ogata *et al.* studied the chemical and physical properties of metal/GO interfaces and observed permeation of Au, Cu, Ni, and Pt into GO films [4.8]. From x-ray photoelectron spectroscopy (XPS) results, two main permeation paths were proposed: 1) metal ion permeation through simultaneous proton exchange; and 2) metal atom permeation via defects and/or edges of GO sheets. Al is a well-known material for its lightweight, good electrical and thermal conductivity, ductility, and corrosion resistance [4.9]. Carbonaceous nanomaterials including graphene have been widely employed as reinforcement materials in Al alloy matrixes to increase its strength while preserving other desirable properties [4.10–4.13]. In addition, Al substrates-graphene films have potential applications in electronic devices [4.14, 4.15]. Previous study of carbon nanotube (CNT) surface in Al matrix has revealed that they are strongly bound by Al – C bond [4.16].

In this paper, we investigate the interfacial development between EPD GO films on Al alloy substrates. Commercially available Al 1100 and Al 5052 plates were chosen as substrates of interest. The composition of Al 1100 is close to that of pure Al, and Al 5052 is corrosion resistance Al alloy with added Mg content. The interfacial chemistry between the substrates with two different compositions are compared. Observations from Fourier-transform infrared spectroscopy (FTIR) and X-ray photoelectron spectroscopy (XPS) have revealed the change in the interfacial chemistry as well as the GO film properties upon heat treatment at 150 °C.

4.4 Experimental Procedures

All chemicals used in the experiments were purchased from Sigma Aldrich, unless otherwise noted. GO sheets were synthesized using modified Hummer's method, as reported elsewhere [4.17]. Briefly, a small amount (~ 0.5 g) of expandable graphite (Grade 1721, Asbury Carbon) was microwaved for 10 s each time to expand the graphite to ~ 150 times of its original volume. Then, 2 g of the produced expanded graphite was slowly added to 200 mL of concentrated H_2SO_4 while mechanically stirring. Furthermore, 15 g of $KMnO_4$ was added to the mixture followed by stirring for 2 hr at 35 °C. After being placed into an ice bath, the mixture received 500 mL of deionized water, added gradually to the mixture. The temperature was maintained below 70 °C. The mixture was stirred for 1 hr followed by dilution with 3.0 L deionized water. After the dilution, 20 mL of H_2O_2 (30 wt. %) was slowly added to the diluted mixture, during which the color of suspension changed from dark brown to yellow. The suspension sat overnight, and the supernatant was decanted. The remaining suspension was centrifuged at 3500 rpm for 15 min followed by a 1 M HCl wash to remove remnant manganese. This was repeated 3 to 4 times. Acid was removed by centrifugation at 12000 rpm for 30 min and a subsequent wash with deionized water for 4 times. The as-synthesized GO dispersion was removed from the centrifugation tube as a highly viscous paste. The paste was dried at 80 °C under vacuum for 24 h. As-prepared GO pasted was suspended in ethanol with desired concentration and ultrasonicated for at least 1 h to disperse the FO flakes evenly in the solution.

EPD of GO was conducted in an electrochemical cell under a parallel pate configuration. GO films were deposited on Al 1100 and Al 5052 plates (McMaster Carr) cut into 2 cm by 4 cm. The compositions of the substrates are presented in Table 4–1. All electrodes were cleaned by ultrasonication in acetone for 20 min followed by acetone and isopropyl alcohol (IPA) to remove impurities. Al 1100 electrodes were purchased with unpolished surface finish and chemically polished to make planar surface, using a method reported elsewhere [4.18]. Briefly, Al 1100 electrodes were dipped in a mixture of 85:15 H_3PO_4 (87 wt. %) and HNO_3 (70 wt. %) at 85 °C for 5 mins followed by neutralization in 1 M NaOH for 5 mins. Al 5052 electrodes were purchased as polished and no further treatment was performed. As the suspension medium, 2.0 mg/ml of GO in ethanol was used. The counter electrode was Al 1100 plate. Deposited samples were dried at room temperature in air for at least 1 hr followed by desiccation. Selected samples were heat treated at a temperature of 150 °C in air.

Table 4–1. Chemical composition limits (max. %) of Al Alloys – Al makes up the remaining composition (From the manufacturer data sheet).

Alloy	Si	Fe	Cu	Mn	Mg	Cr	Zn	Ti	Other
1100	1.0 (Si+Fe)		0.2	0.05	0.05	-	0.1	0.6	0.15
5052	0.25	0.7	0.1	0.1	2.8	0.35	0.2	-	0.15

The electrophoretic mobility and zeta potential of the GO suspension were measured with a Malvern Zetasizer Nano S dynamic light scattering (DLS) system. Specimens were observed using optical microscopy and scanning electron microscopy (SEM, Hitachi S-4800 and S-3200) to probe their microstructure. Fourier transform infrared spectroscopy (FT-IR, Thermo Scientific Nicolet 6700) was used to assess the chemical characteristics of the films. The obtained FT-IR spectra were baseline corrected with data processing software (OMNIC, Thermos Scientific). X-ray photoelectron spectroscopy (Al Kα XPS, Thermos Scientific) was used to assess atomic composition and interfacial characteristics. The X-ray source had a spot size of 400 μm. For depth profiling, the GO films were etched with Ar ion with 3 keV. The obtained XPS spectra were peak fitted by using Avantage data analysis system (Thermos Scientific) with Gaussian and/or Lorentzian peak shapes.

4.5 Results and Discussions

The electrophoretic mobility of the GO sheets in ethanol was –0.4325 μm-cm/V-s as shown in Figure 4–1(a). Negative mobility of the colloidal GO sheets was confirmed again by formation of anodic deposits. Figure 4–1 (b) shows a typical current density plot of EPD of GO on Al alloys respectively. An exponential decaying of current density as a function of time was observed for each of the samples. Such a decreasing current density is due to the evolution of the multi-component impedance (capacitance and resistance) of the system: the changing impedance of the GO film cast on each electrode and the evolving impedance of the suspension [4.6]. The curves also present well-controlled EPD process without significant fluctuations in current density caused by gas evolution or reduction of GO at the electrode surface [4.6].

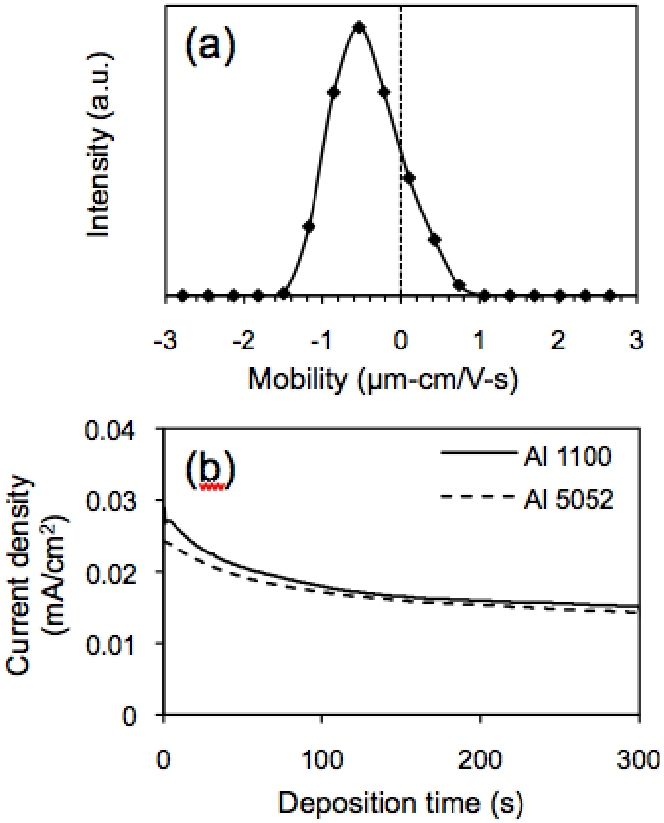

Figure 4–1. (a) Electrophoretic mobility plot of 2.0 mg/ml GO suspension in pure ethanol, (b) Current density plot of EPD-GO on Al 1100 and Al 5052 substrates

Figure 4–2 (a) and (c) show photographs of samples pre- and post- heat treatment process, respectively. Reduction of the deposited GO films was confirmed by a color change from light brown to black after the heat treatment. SEM micrographs of sample surfaces, pre- and post- heat treatment, are presented in Figure 4–2 (b) and (d), respectively. The as deposited GO films consist of nearly flat stacks of GO with occasional wrinkle-like structures. Similar microstructure has been observed in previous studies on EPD GO [4.3, 4.6]. The wrinkling can be due to overlapping of the individual sheets, distortions of the tetrahedral carbon plane due to –OH defects [4.6, 4.17], and even due to substrate impurities. After the heat treatment, these wrinkles were almost flattened out, as depicted in Figure 4–2 (d). This could be due to stress relaxation of the overlapped GO sheets upon heat treatment. The microstructure of GO films deposited on Al 1100 and Al 5052 substrates had no significant difference.

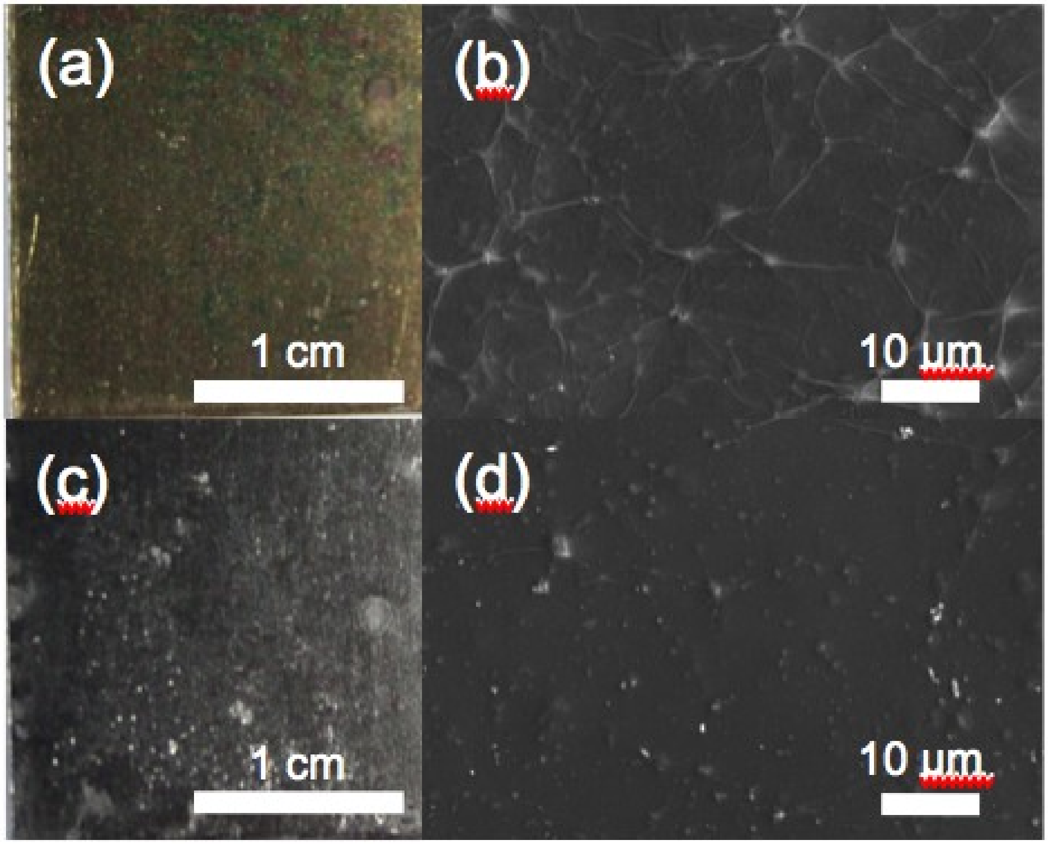

Figure 4–2. Photograph and SEM images of GO deposited on Al 1100 – (a,b) as-deposited, (c,d) after heat treatment at 150 °C.

Figure 4–3 compares obtained FT-IR spectra of GO films on Al 1100 substrates and freestanding GO films. All of the FT-IR spectra in Figure 4–3 (a) and (b) have broad peaks at ~ 3380 cm^{-1}, which are from free –OH groups in deposited GO films. After the heat treatment, the –OH peaks dramatically decreased, as seen in Figure 4–3 (c) and (d). The FT-IR spectra of GO films on Al substrates (GO/Al) were compared with that of the freestanding GO films to observe extant peak shifts. Detailed peak assignments for the obtained spectra are listed in Table 4–2. Sharper peaks at ~1650 cm^{-1} and ~1380 cm^{-1} were observed for the GO/Al samples, which correspond to the asymmetric and symmetric C–O peaks, respectively, although overlapping peaks reside within the same regions. The appearance of the two peaks is due to the deprotonation of C=O and C–O groups in carboxyl and may be evidence for the formation of bonds between aluminum metal and oxygen. Frequency differences (Δν) between the asymmetric and the symmetric peaks can reveal the coordination of the chemical bond. The difference can range from approximately 100 cm^{-1} to 300 cm^{-1}, increasing as the coordination changes from bidentate to monodentate [4.20]. Noticeable changes in peaks were observed after the heat treatment of GO/Al. The $\Delta\nu$ between the two peaks had changed from ~250 cm^{-1} to ~124 cm^{-1}, which indicates a change in the bond coordination after heat treatment.

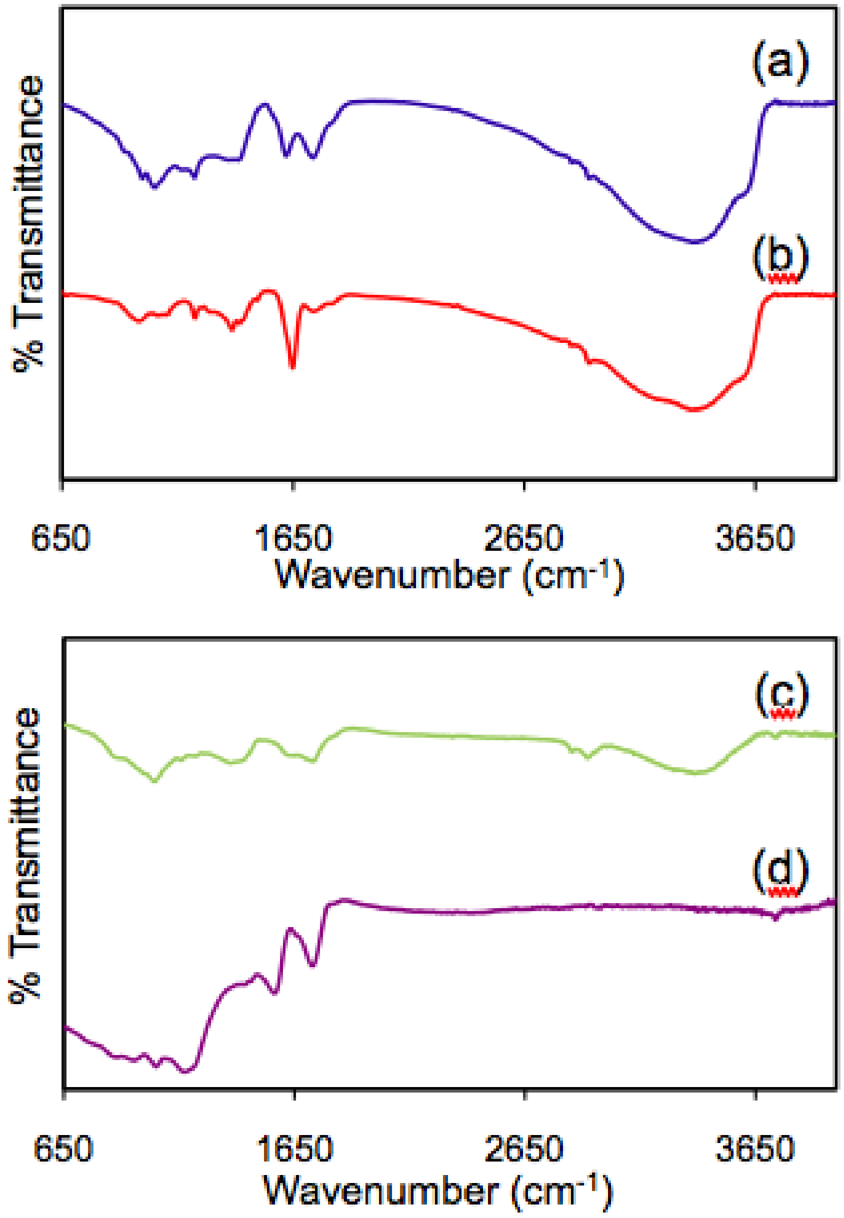

Figure 4–3. FT-IR spectra – (a) Free-standing GO, (b) GO on Al 1100, (c) free-standing GO after heat treatment, and (d) GO on Al 1100 after heat treatment.

Table 4–2. FT-IR spectra peak assignments.

Free-standing GO	GO/ Al 1100	Free-standing rGO	rGO/ Al 1100	Assignments
1735 cm^{-1}	1740 cm^{-1}	1733 cm^{-1}	1729 cm^{-1}	ν (C = O)
1619 cm^{-1}	1649 cm^{-1}	1653 cm^{-1}		ν (as. C – O) C = C (aromatic ring)
			1559 cm^{-1}	
		1507 cm^{-1}		def.(C – C)
			1435 cm^{-1}	ν(s. C – O) + def.(O – H) combination
1414 cm^{-1}	1417 cm^{-1}		1411 cm^{-1}	
1392, 1374 cm^{-1}	1384 cm^{-1}	1372 cm^{-1}		
1223 cm^{-1}	1225 cm^{-1}	1223 cm^{-1}		ν(C – O) from COOH
1174 cm^{-1}		1158 cm^{-1}	1172 cm^{-1}	ν(C – O) epoxy or δ(C – H)
1053 cm^{-1}	1058 cm^{-1}	1044 cm^{-1}	1049 cm^{-1}	ν(C – O) alkoxy
999 cm^{-1}	982 cm^{-1}		958 cm^{-1}	cyclohexane

To observe changes in the bonding chemistry from surfaces to film–substrate interfaces, XPS depth profile analyses were performed on each specimen. Figure 4–4 (a) is a schematic diagram of approximate points at which the XPS analyses depicted in Figure 4–4 (b) and (c) were acquired. All presented spectra have been normalized for ease of comparison. The C 1s spectra of GO have four main peaks: C–C from graphitic carbon at 284.6 eV; C–O from hydroxyl and epoxide at 286 eV; C=O at 287 eV; and COOH and COOR at 289 eV [4.21, 4.22]. An extended tail observed at 291 eV is from π–π^* carbon interactions [4.22]. C/O ratios for each specimen are listed in Table 4–3. For all samples, a reduction in oxygen-containing groups was observed after removal of the surface layer. Although the reduction of GO films during EPD has been reported previously [4.2, 4.4], we suspect Ar ion bombardment to remove surface layer during the XPS depth profiling process is the main contributor to the reduction of oxygen. Even low energy Ar ions are sufficient to remove oxygen from GO films [4.23, 4.24]. Previous studies have revealed that the reduction due to Ar ion bombardment occurs in the first several minutes with ~ 20 °C temperature increase, which is not enough for thermal deoxygenation [4.24]. Ar does not chemically react with GO films [4.23]. Oxygen removal from the Ar etch is only from physical processes. The atomic concentration of oxygen is highly affected by Ar bombardment; however, chemical bonding information obtained at each etch level remained reliable.

Table 4–3. Averaged C/O ratio of GO on Al 1100.

	As-deposited	Heat treated
Film Surface	2.52	3.95
After Ar etch	~18	~18

Interpretation of the O 1s spectra is rather difficult as many peaks closely overlap in the region from 531 eV to 534 eV. The following peak assignments were guided by assignments from previous studies, all motivated to obtain the best fit: C=O at 531.1 eV; metal oxide and C–OH at 531.9 eV; C–O–C and ether oxygen at 532.8 eV; and COOH/COOR at 534.1 eV [4.22]. A low intensity broad peak at 536.2 eV is from adsorbed water, which is in accordance with peaks at ~ 78 eV and ~ 1306 eV for metal binding to adsorbed water in Al 2p and Mg 1s spectra, respectively [4.25]. An example of the O 1s peak fitting at different depth is shown in Figure 4–4(c). A dramatic decrease, observed in the C–OH signal after etching the surface away, is congruent with the change in the C 1s spectra, as presented in Figure 4–5(b). Throughout the GO film, the O 1s spectra reflected the superposition of four mixed states, characterized by the convolution of four different peaks. No significant change in the elemental composition or chemical state was observed inside the films. However, near the film/substrate interface, the C=O peak at 531 eV decreased with no significant change in the COOH/COOR peak or the ether oxygen peak. This change suggests possible breakage of the C=O bond eventually creating a C–O–Al bond structures highlighting further need of high-resolution XPS survey of Al spectra . The high-resolution C 1s and O 1s spectra at all depths for GO films deposited on Al 1100 and Al 5052 substrates had significant difference such as peak shifts or appearance of a new peak.

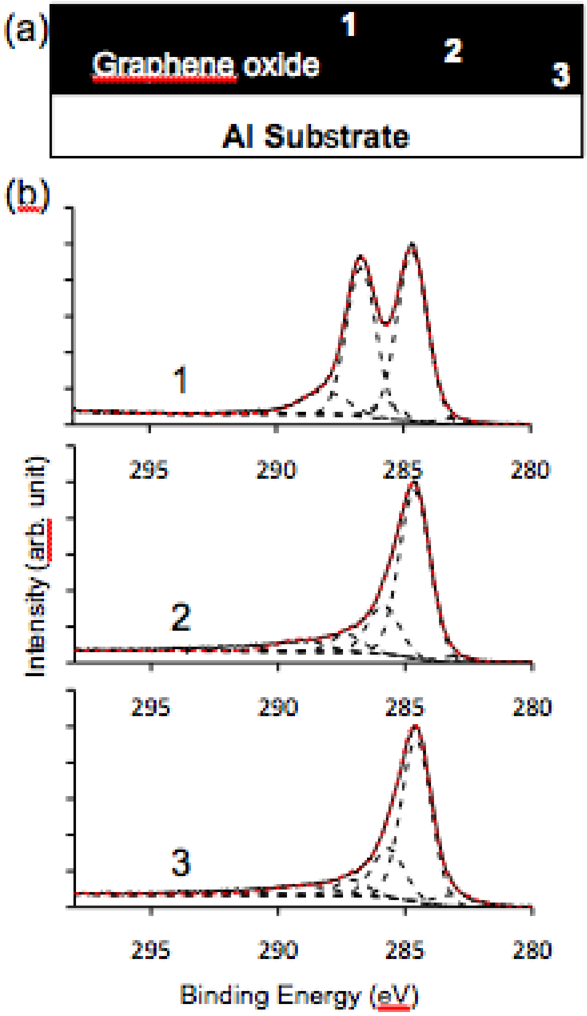

Figure 4–4. XPS depth profile – (a) Schematic diagram of point of analyses, (b) C 1s spectra of EPD GO on Al 1100, and (c) O 1s spectra of EPD GO on Al 1100.

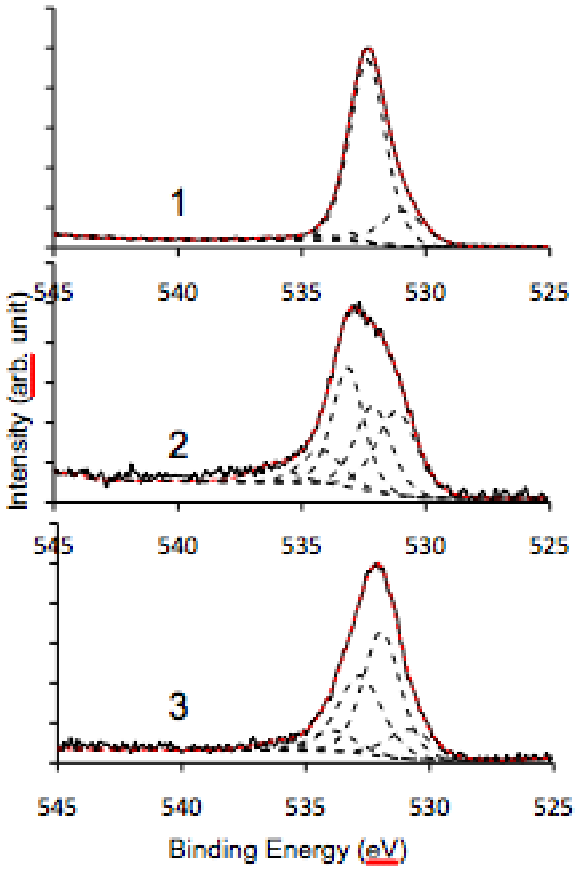

Metal permeation into the GO was present in all specimens. High-resolution Al 2p spectra in Figure 4–5 (a) were dominated by the Al–O peak at ~74.5 eV. After heat treatment, the Al–O peak shifted towards 75 eV, which indicates a change in chemical state. In previous studies of the Al and polymer interface, peaks at ~74.5 eV were considered to be from the Al–O–C bond instead of the Al–O originating from the native aluminum oxide layer [4.26, 4.27]. For Al 5052 substrates, additional Mg peak was detected and high-resolution Mg spectra are displayed in Figure 4–5(b). The Mg 1s spectra in Figure 4–5 (b) had noticeable peak shifts at the film surfaces towards metallic Mg. Except at the surface level, all depth levels had peaks at ~1304 eV, which can be attributed to MgO or Mg^{2+}. From these results, the permeation of Al and Mg into GO films certainly arose from proton exchange rather than permeation of metal atoms [4.8]. The amount of Mg present across the different levels within the stacked GO sheets persisted at ~ 0.7 at. %. In contrast, the Al ions were distributed unevenly in a range of 0 at % and 2.0 at %. This discrepancy in the Al distribution waned after heat treatment of the samples. From previous studies of metal permeation into GO, the distribution of metal atoms or ions largely depends upon metal-carbon bonding strength, and the transport is perturbed when a bond is made between C(O)O and a metal atom [4.8]. Therefore, Al is likely the major contributor in the adhesion of GO films to their underlying Al-based substrates rather than Mg in such Al–Mg alloys.

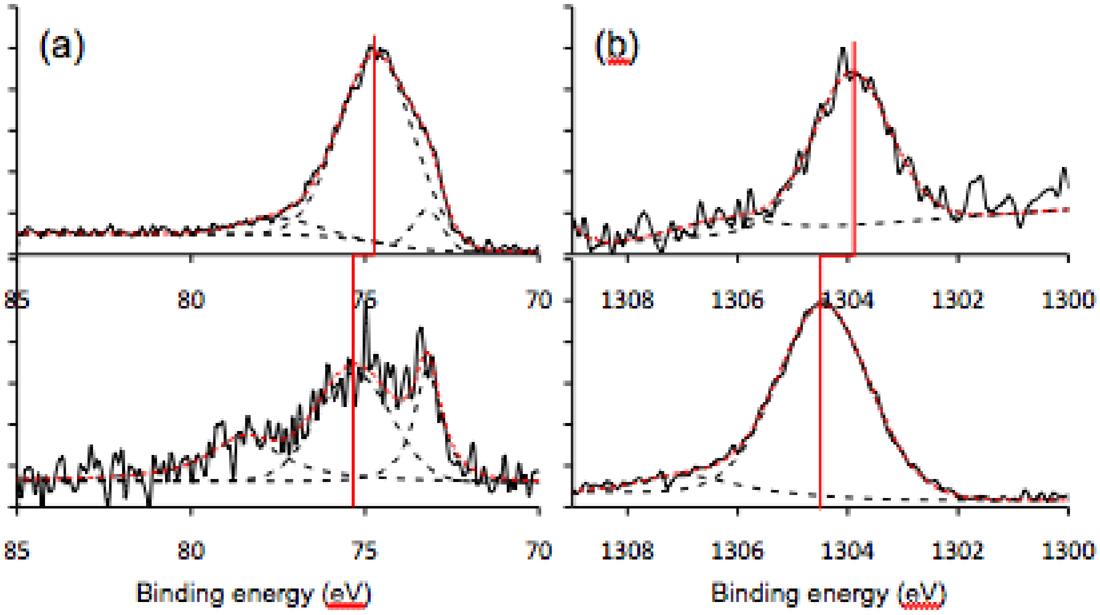

Figure 4–5. High resolution XPS spectra from EPD GO on Al 5052 – (a) Al 2p and (b) Mg 1s; top – before heat treatment, bottom – after heat treatment.

4.6 Conclusions

In conclusion, the chemical properties of EPD GO films on Al 1100 and Al 5052 substrates were investigated using FT-IR and XPS depth profiling. The results confirmed the formation of Al–O–C bonds between the films and both Al-based substrates. Moreover, metal ion permeation into the GO films was observed. Upon heat treatment, the evolution of the chemical structure of the films, specifically involving the metal atoms, was evidenced from peak shifts observed in high-resolution XPS spectra of Al and Mg. Finally, these findings provide considerable information about chemical interactions between GO films and Al alloy substrates during EPD and heat treatment processes, which is important in optimizing the sustained adhesion of GO films onto their underlying substrates for functional coating applications.

Acknowledgements

Author would like to thank Fonds de Recherche – Nature et Technologies (FQRNT) and Aluminium Research Centre – REGAL for their financial supports. Research was carried out in part at the Center for Functional Nanomaterials, Brookhaven National Laboratory, which is supported by the U.S. Department of Energy, Office of Basic Energy Sciences, under Contract No. DE-SC0012704.

4.7 References

4.1. Chavez-Valdez, A., M.S.P. Shaffer, and A.R. Boccaccini, *Applications of Graphene Electrophoretic Deposition. A Review.* Journal of Physical Chemistry B, 2013. **117**(6): p. 1502-1515.

4.2. Ishikawa, R., et al., *Electrophoretic deposition of high quality transparent conductive graphene films on insulating glass substrates.* Asia-Pacific Interdisciplinary Research Conference 2011 (Ap-Irc 2011), 2012. **352**.

4.3. Hasan, S.A., et al., *Transferable Graphene Oxide Films with Tunable Microstructures.* Acs Nano, 2010. **4**(12): p. 7367-7372.

4.4. An, S.J., et al., *Thin Film Fabrication and Simultaneous Anodic Reduction of Deposited Graphene Oxide Platelets by Electrophoretic Deposition.* Journal of Physical Chemistry Letters, 2010. **1**(8): p. 1259-1263.

4.5. Chen, Y., et al., *Electrophoretic deposition of graphene nanosheets on nickel foams for electrochemical capacitors.* Journal of Power Sources, 2010. **195**(9): p. 3031-3035.

4.6. Diba, M., et al., *Quantitative evaluation of electrophoretic deposition kinetics of graphene oxide.* Carbon, 2014. **67**: p. 656-661.

4.7. Hamaker, H.C., *Formation of a deposit by electrophoresis.* Transactions of the Faraday Society, 1940. **35**(3): p. 0279-0286.

4.8. Ogata, C., et al., *Metal Permeation into Multi-layered Graphene Oxide.* Scientific Reports, 2014. **4**.

4.9. Davis, J.R., *Corrosion of aluminum and aluminum alloys*1999, Materials Park, OH: ASM International. vii, 313 p.

4.10. Bartolucci, S.F., et al., *Graphene-aluminum nanocomposites.* Materials Science and Engineering a-Structural Materials Properties Microstructure and Processing, 2011. **528**(27): p. 7933-7937.

4.11. Perez-Bustamante, R., et al., *Microstructural and hardness behavior of graphene-nanoplatelets/aluminum composites synthesized by mechanical alloying.* Journal of Alloys and Compounds, 2014. **615**: p. S578-S582.

4.12. Wang, J.Y., et al., *Reinforcement with graphene nanosheets in aluminum matrix composites.* Scripta Materialia, 2012. **66**(8): p. 594-597.

4.13. Yan, S.J., et al., *Investigating aluminum alloy reinforced by graphene nanoflakes.* Materials Science and Engineering: A, 2014. **612**(0): p. 440-444.

4.14. Lee, S.H., et al., *Reduced graphene oxide coated thin aluminum film as an optoacoustic transmitter for high pressure and high frequency ultrasound generation.* Applied Physics Letters, 2012. **101**(24).

4.15. Cho, B., et al., *Graphene-based gas sensor: metal decoration effect and application to a flexible device.* Journal of Materials Chemistry C, 2014. **2**(27): p. 5280-5285.

4.16. So, K.P., et al., *Electroplating formation of Al-C covalent bonds on multiwalled carbon nanotubes.* Synthetic Metals, 2011. **161**(3-4): p. 208-212.

4.17. Pham, V.H., et al., *Fast and simple fabrication of a large transparent chemically-converted graphene film by spray-coating.* Carbon, 2010. **48**(7): p. 1945-1951.

4.18. Alam, K.M., et al., *Fabrication of hexagonally ordered nanopores in anodic alumina: An alternative pretreatment.* Surface Science, 2011. **605**(3-4): p. 441-449.

4.19. Lerf, A., et al., *Structure of graphite oxide revisited.* Journal of Physical Chemistry B, 1998. **102**(23): p. 4477-4482.

4.20. Crowell, J.E., J.G. Chen, and J.T. Yates, *The Adsorption and Decomposition of Carboxylic-Acids on Al(111).* Journal of Electron Spectroscopy and Related Phenomena, 1986. **39**(1-4): p. 97-106.

4.21. Yang, D., et al., *Chemical analysis of graphene oxide films after heat and chemical treatments by X-ray photoelectron and Micro-Raman spectroscopy.* Carbon, 2009. **47**(1): p. 145-152.

4.22. Boudou, J.P., et al., *Oxygen plasma modification of pitch-based isotropic carbon fibres.* Carbon, 2003. **41**(1): p. 41-56.

4.23. Baraket, M., et al., *Reduction of graphene oxide by electron beam generated plasmas produced in methane/argon mixtures.* Carbon, 2010. **48**(12): p. 3382-3390.

4.24. Zhou, Q., et al., *Low temperature plasma-mediated synthesis of graphene nanosheets for supercapacitor electrodes.* Journal of Materials Chemistry, 2012. **22**(13): p. 6061-6066.

4.25. Abreu, C.M., et al., *Passive layers developed on different tempers of AA7075 aluminium alloy after molybdenum implantation.* Surface and Interface Analysis, 2012. **44**(8): p. 1039-1044.

4.26. Ho, P.S., et al., *Chemical Bonding and Reaction at Metal Polymer Interfaces.* Journal of Vacuum Science & Technology a-Vacuum Surfaces and Films, 1985. **3**(3): p. 739-745.

4.27. Underhill, R. and R.S. Timsit, *Interaction of Aliphatic-Acids and Alcohols with Aluminum Surfaces.* Journal of Vacuum Science & Technology a-Vacuum Surfaces and Films, 1992. **10**(4): p. 2767-2774.

CHAPTER 5

Dynamic Mechanical Characterization of Electrophoretically Deposited Graphene Oxide Films on Al 5052

Sumin Jin [1], Viet Hung Pham [2], Abhi Ghosh [1], James H. Dickerson [2,3], Mathieu Brochu [1]

[1] Department of Mining and Materials Engineering, McGill University, Montreal, QC
[2] Center for Functional Nanomaterials, Brookhaven National Laboratory, Upton, NY, USA
[3] Department of Physics, Brown University, Providence, RI, USA

5.1 Preface

In order to apply EPD graphene oxide for coating and device applications, understanding mechanical properties of graphene oxide film/substrate system is important. Materials are more likely to undergo dynamic deformation in manufacturing process and usage. Recently developed Nano-impact testing enables characterization of dynamic mechanical properties of coated system in nano-scale. The following chapter contains results from Nano-impact testing of EPD graphene oxide films on Al 5052 substrates at various impact velocities. Films on Al 5052 substrates were chosen because of the best adhesion among the three Al alloy substrates. Moreover, the chapter explains deformation behavior of graphene oxide films upon high-strain rate localized impact.

5.2 Abstract

Dynamic mechanical property of electrophoretically deposited (EPD) graphene oxide (GO) films on Al 5052 alloys is investigated via Nano-impact testing technique. GO films with thicknesses ranging from ~ 600 nm to 1700 nm were tested for single dynamic impact response with loads in a range of 0.1 mN and 10 mN. Coefficient of restitution, dynamic energy change, and dynamic hardness values were calculated. Al 5052 with GO films demonstrated ability to damp out and

dissipate high impact energy implying potential application of graphene-based coatings in dynamic environment.

5.3 Introduction

Carbonaceous nanomaterials are promising for a wide range of applications due to their superior electronic, mechanical and magnetic properties. Graphene is a sheet of carbon atoms in 2D honeycomb lattice structure and has attracted many scientists because of its sheet-like structure with high aspect ratio (lateral size to thickness) [5.1]. Particularly, pristine graphene has superior mechanical properties with Young's modulus of 1.0 ± 0.1 TPa and intrinsic strength of 130 ± 10 GPa [5.2]. However, low yield of pristine graphene from mechanical exfoliation is the major drawback for mass production. Chemical synthesis of graphene oxide (GO) is a promising route of producing graphene-based materials with high yield and low cost [5.3]. Unlike pristine graphene, GO is heavily decorated with oxygen bearing functional groups that act as structural defects. Theoretical evaluation has revealed the oxidative defects on GO surface notably decreases in-plane Young's modulus but have no significant influence in fracture strength [5.4]. Previous studies on mechanical behavior of graphene and GO were mostly carried out under quasi-static conditions [5.2, 5.5-5.9]. Experimental results using AFM nanoindentation technique gave Young's modulus of GO ranging from 100 GPa to 400 GPa depending on film thicknesses and production techniques [5.5, 5.8, 5.9]. More precise measurements using nanoindentation with dynamic contact module (DCM) system gave slightly higher Young's modulus ranging from 695 ± 53 GPa and 697 ± 15 GPa with ultimate tensile strength from 11 and 8 GPa at film thicknesses of 50 nm and 60 nm, respectively [5.7]. Direct comparison of GO's mechanical properties is difficult because the amount of the surface oxygen bearing groups and film thickness affect the material response. From previous studies, Young's modulus decreased with increasing number of stacked GO layers, which is in line with the reduction of mechanical properties with bundling of single-walled carbon nanotubes [5.5, 5.6, 5.10].

In real-life applications, materials are more likely to undergo deformation in dynamic conditions [5.11]. Thus, it is essential to investigate dynamic mechanical properties of graphene and GO.

Lee and co-workers performed laser induced projectile impact test (LIPIT) on free-standing multilayer graphene [5.12]. They suspended multilayer graphene films produced by mechanical exfoliation with thicknesses ranging from 10 nm to 100 nm onto a grid sample holder. From the experimental results, multilayer graphene displayed significantly better ability to delocalized impact energy than Kevlar armor material. This implies potential application of graphene-based material as shock absorbers. Mechanical properties of GO have never been studied under dynamic condition, thus understanding dynamic mechanical properties of GO will help elucidate the effect of structural defects on its ability to dissipate impact energy.

Herein, we report dynamic mechanical study of GO films on Al alloy substrates. Al-based alloy was chosen as substrate materials due to their broad spectrum of applications and desirable properties including lightweight, good electrical and thermal conductivity, and corrosion resistance [5.13]. However, Al is known to have poor energy dissipation upon high impact [5.14]. Energy dissipation capability of graphene-based coating can improve mechanical properties of Al, which will perpetuate the use of Al alloys as structural materials in dynamic environment. GO films with thicknesses ranging from ~ 660 nm to 1700 nm were deposited via electrophoretic deposition (EPD) technique. High-strain rate nano-impact testing was performed. Nano-impact testing enables dynamic mechanical characterization in nano- and micro- meter regimes with high sampling rate, which enables testing in more controlled manner [5.15]. Microstructures of deposited films and post-mortems from the impact tests were observed via scanning electron microscopy (SEM). From the impact tests, coefficient of restitution, dynamic energy dissipation and dynamic hardness of GO were calculated.

5.4 Experimental

All chemicals used in this study were purchased from Sigma Aldrich, otherwise noted. GO was synthesized using modified Hummer’s method reported elsewhere [5.16]. The GO films were deposited on Al 5052 plates (McMaster Carr) by EPD technique in a parallel two-electrodes cell. Composition of the substrate from the manufacturer data sheet is presented in Table 5–1. All substrates were cleaned by ultrasonication in Acetone for 20 min followed by Acetone and

Isopropyl Alcohol (IPA) wash to remove impurities on the surfaces. Samples were deposited in a solution containing 2.0 mg/ml of GO in ethanol at 10 V for deposition times ranging from 5 min to 30 min. Deposition area was ~ 2 cm^2, and commercial pure Al plate was used as a counter electrode. All specimens were dried at room temperature in air for at least 1 hr after the deposition followed by desiccation.

Table 5–1. Wt. % composition of Al 5052 alloy (from Manufacturer data sheet).

Si	Fe	Cu	Mn	Mg	Cr	Zn	Other
0.25	0.7	0.1	0.1	2.8	0.35	0.2	0.15

Specimens were observed with optical microscopes and SEM (Hitachi SU-3200) for their microstructure and post–mechanical testing artifacts. X-ray photoelectron spectroscopy (XPS Al Kα, Thermos Scientific) was performed on the surfaces to obtain carbon to oxygen (C/O) ratio. Samples with three different average film thicknesses, namely 662 ± 123 nm, 1320 ± 185 nm, and 1706 ± 178 nm were tested for dynamic hardness using nano-impact testing (NanoTest 3, Micromaterials) with cube-corner tip. Films were tested at 7 different impact loads. Impact velocity is calculated from detected pendulum movement with sampling rate of 8 kHz. Impact velocities at the each applied load are listed in Table 5–2. The applied velocities were within 2 % error. At least five different sample locations were tested at each load. Dynamic hardness was calculated as per equation 5.1 [5.16],

$$H_d = \frac{3m(v_{in}^2 - v_{out}^2)}{2\alpha h_r^3} \tag{5.1}$$

where m is mass of pendulum, v_{in} is impact velocity, v_{out} is rebound velocity, α is indenter geometry parameter, and h_{res} is residual depth. The mass of pendulum is 0.240 g and the indenter geometry parameter for a cube-corner tip is 2.59. A more complete description of the testing procedure can be found in [5.16].

Table 5–2. Applied loads with corresponding impact velocity.

Load (mN)	V_{in} (mm/s)
0.1	0.288
0.5	0.337
1.0	0.392
2.5	0.512
5.0	0.669
7.5	0.796
10.0	0.896

5.5 Results and Discussions

Cross-sectional and surface SEM micrographs of the deposited GO films are presented in Figure 5–1 (a) and (b) respectively. The films consist of stacked sheets of GO from the cross-sectional view. Some wrinkling of GO sheets could be observed on the surface due to overlapping and aggregation of colloidal GO. Other than sporadic wrinkles, GO sheets were lying flat on the surface. Similar microstructure has been observed in previous studies of EPD GO [5.17–5.20]. The XPS analysis revealed an average C/O ratio for the EPD GO films of 2.29. Figure 5–1 (c) and (d) depict post-impact SEM micrographs of 1320 nm of GO film at 0.1 mN and 7.5 mN respectively. After an impact at low loads below 1 mN, the films were folded towards the indenter edge forming a pile up. There was no apparent crack formation observed at low loads. At high impact loads, cracks started to grow from the film surface. In addition, GO films slid in outward direction forming creases caused by elastic waves from the impacts [5.12].

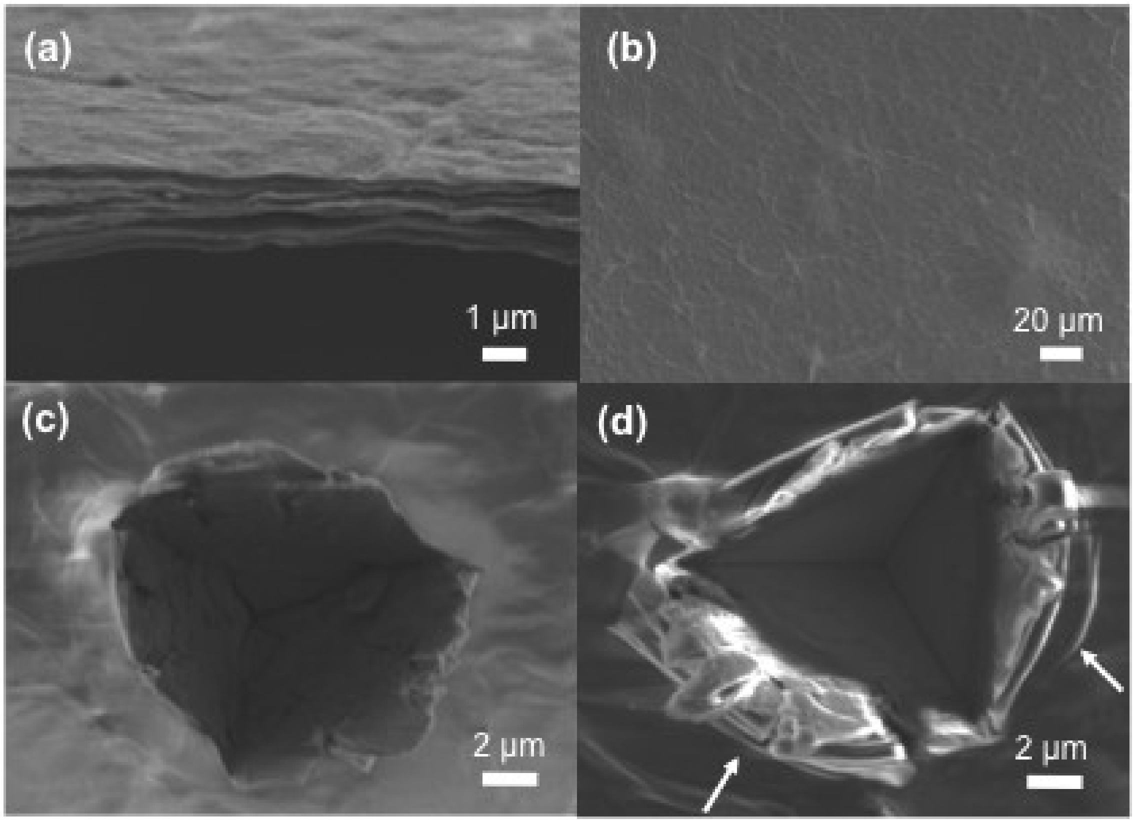

Figure 5–1. SEM micrographs – (a) cross-sectional view and (b) top-down view of deposited GO films, top-down view of post-impact areas of 1320 nm GO film on Al 5052 at impact load of (c) 0.1 mN and (d) 7.5 mN.

Displacement plots obtained during nano-impact testing provide information regarding pendulum movement after a high strain-rate impact. The pendulum rebound depends on energy loss from testing material, the instrument, and the indenter tip geometry [5.15]. Figure 5–2(a) compares the acquired displacement data for the Al substrate and of the three specimens with different film thicknesses at 0.1 mN. The Al substrate displayed poor damping of the pendulum displacement after an impact compared to the specimens with GO films. With increasing film thickness, the number of rebounds decreased due to less substrate contribution to the experimental data. The curves indicate that impact energy loss is primarily from the GO films. Collision characteristic of the first rebound can be quantified by calculating coefficient of restitution, e as per equation 5.2 [5.16].

$$e = \left| \frac{v_{out}}{v_{in}} \right| \tag{5.2}$$

The coefficient of restitution reaches 1 for a purely elastic collision, where no kinetic energy is lost, and 0 for a purely plastic collision. Figure 5–2(b) depicts coefficient of restitution for all samples at different impact loads. For all specimens, e was in a range of approximately 0.3 and 0.4. Change in e with respect to loads was statistically insignificant for all samples. Samples with thick GO films had lower coefficient restitution at low loads and reached close to the substrate value at high loads due to substrate contribution. Lower coefficient of restitution of the thick GO films correlates well with the decrease in number of rebounds for GO films displayed in Figure 5–2(a). Comparing with the large number of rebouds from bare Al substrate, we can say that the decrease in the number of rebounds and lower coefficient of restitution should be due to the GO films. The dissipated energy from dynamic response of material, $\Delta E_{dynamic}$ can be quantified by subtracting plastic work of deformation, $W_{plastic}$ from change in kinetic energy, ΔE_k as per equation 3 [5.21].

$$\Delta E_{dynamic} = \Delta E_k - W_{plastic} \tag{3}$$

ΔE_k and $W_{plastic}$ are obtained from equation 4 and 5 respectively,

$$\Delta E_k = \frac{1}{2} m (v_{in}^2 - v_{out}^2) \tag{4}$$

$$W_{plastic} = \int_0^{h_{res}} F \cdot dx \tag{5}$$

where F is resistive force of the material calculated from deceleration during an impact and x is change in indentation depth. Figure 5–2(c) compares $\Delta E_{dynamic}$ of GO films at different thicknesses in the range of tested impact loads. Percentage of kinetic energy dissipated as dynamic energy was 22 ± 8 % and 50 ± 12 % for Al 5052 and 1704 nm GO film on Al 5052 substrate at 0.1 mN respectively. At low impact loads, where most of impact energy was concentrated on the GO films, the dynamic energy dissipation was double the bare substrate. Considering extremely small density of GO around 1.32 mg/cm^3 [5.22], GO films have very large dynamic energy dissipation per density. As the indenter tip penetrates the GO film at high impact loads, the amount of dynamic energy dissipation reached close to that of Al 5052 for 662 nm GO films. However, GO films with thickness of 1320 nm and 1706 nm maintained larger dynamic energy dissipation than Al 5052 even at the highest tested impact load of 10 mN. Figure

5–2 (d) shows dynamic hardness values, calculated using equation 1, over film thickness normalized residual depths for the samples. The color code relates to the impact loads.

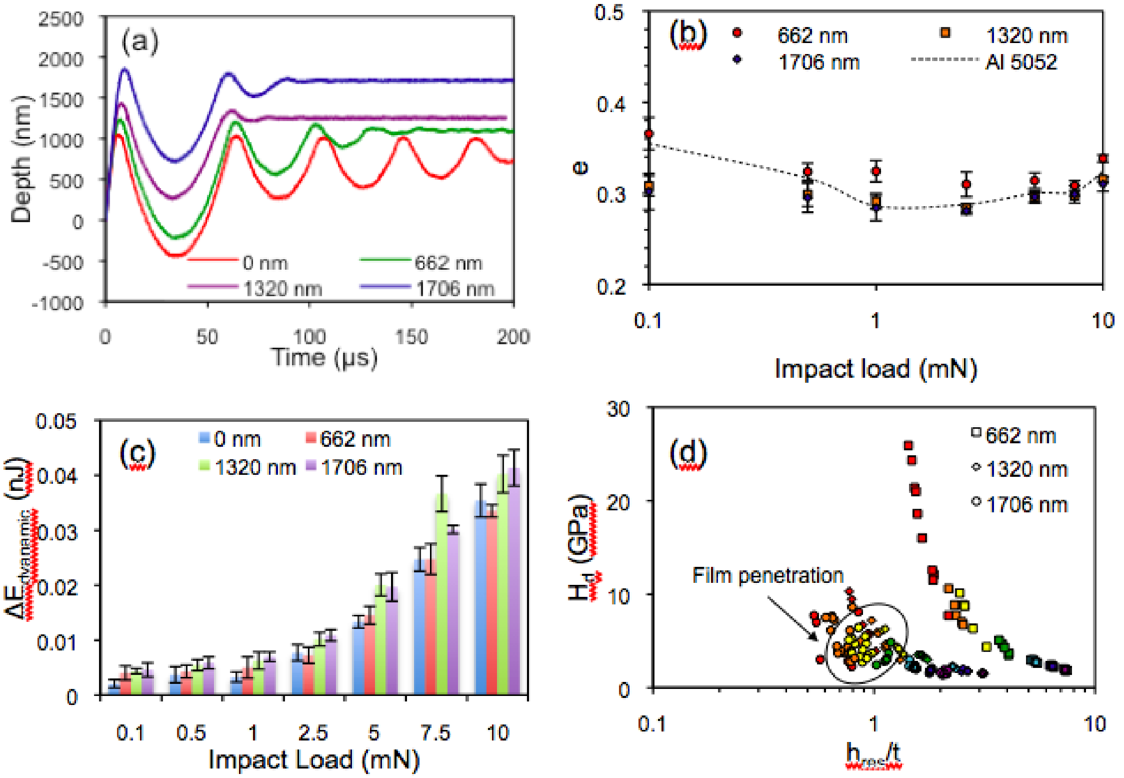

Figure 5–2. (a) displacement vs. time plot, (b) coefficient of restitution vs. impact load plot, (c) dynamic energy dissipation vs. impact load plot and (d) dynamic hardness vs. film thickness normalized residual depth – 0.1 mN (Red), 0.5 mN (Orange), 1 mN (Yellow), 2.5 mN (Green), 5 mN (Blue), 7.5 mN (Navy), 10 mN (Purple).

Dynamic hardness of the all three specimens reached the substrate value of 1.57 GPa with increasing impact load. The obtained results deviate from the linear shaped Nix-Gao relation of indentation hardness and display exponential decrease. This was discussed in details in a previous study [5.23]. The exponential decrease is due to adiabatic localized heat generation and subsequent softening of the material at high impact load [5.21]. GO film with thickness of 662 nm was completely penetrated by the indenter tip at the lowest impact load of 0.1 mN. Thus, extremely high dynamic hardness values at low depths (i.e. low impact loads) are primarily due to strain hardening of Al 5052. Samples with 1320 nm and 1706 nm of GO films had lower dynamic hardness values at loads below 2.5 mN. The scattering near the film–substrate interface would be due to penetration of the films and partial delamination of films due to crack formation in the top layers. The dynamic hardness with penetration depth close to the interface was ~ 4 GPa in average for both 1320 nm and 1706 nm films.

5.6 Conclusions

In conclusion, we performed Nano-impact tests on EPD GO films on Al 5052 substrates. Upon localized impact, collision characteristic of specimens with GO films was relatively plastic compared to bare Al 5052 substrates where the film immediately damped out movement of the collided pendulum. With the least substrate contribution, Al 5052 with GO films dissipated twice the dynamic energy compared to bare Al 5052 substrates. Specimens with GO films thicker than 1 μm displayed better dynamic energy dissipation than the bare substrate at all loads between 0.1 mN and 10 mN. The study suggests potential application of GO coatings in dynamic environment.

Acknowledgements

Author would like to thank Fonds de Recherche – Nature et Technologies (FQRNT) and Aluminium Research Centre – REGAL for their financial supports. Research was carried out in part at the Center for Functional Nanomaterials, Brookhaven National Laboratory, which is supported by the U.S. Department of Energy, Office of Basic Energy Sciences, under Contract No. DE-SC0012704.

5.7 References

5.1. Wu, Z.S., et al., *Field Emission of Single-Layer Graphene Films Prepared by Electrophoretic Deposition.* Advanced Materials, 2009. **21**(17): p. 1756-+.

5.2. Lee, C., et al., *Measurement of the elastic properties and intrinsic strength of monolayer graphene.* Science, 2008. **321**(5887): p. 385-388.

5.3. Diba, M., et al., *Quantitative evaluation of electrophoretic deposition kinetics of graphene oxide.* Carbon, 2014. **67**: p. 656-661.

5.4. Paci, J.T., T. Belytschko, and G.C. Schatz, *Computational studies of the structure, behavior upon heating, and mechanical properties of graphite oxide.* Journal of Physical Chemistry C, 2007. **111**(49): p. 18099-18111.

5.5. Gomez-Navarro, C., M. Burghard, and K. Kern, *Elastic properties of chemically derived single graphene sheets.* Nano Letters, 2008. **8**(7): p. 2045-2049.

5.6. Kang, S.-H., T.-H. Fang, and Z.-H. Hong, *Electrical and mechanical properties of graphene oxide on flexible substrate.* Journal of Physics and Chemistry of Solids, 2013. **74**(12): p. 1783-1793.

5.7. Kang, S.H., et al., *Mechanical properties of free-standing graphene oxide.* Diamond and Related Materials, 2013. **38**: p. 73-78.

5.8. Robinson, J.T., et al., *Wafer-scale Reduced Graphene Oxide Films for Nanomechanical Devices.* Nano Letters, 2008. **8**(10): p. 3441-3445.

5.9. Suk, J.W., et al., *Mechanical Properties of Monolayer Graphene Oxide.* Acs Nano, 2010. **4**(11): p. 6557-6564.

5.10. Salvetat, J.P., et al., *Elastic and shear moduli of single-walled carbon nanotube ropes.* Physical Review Letters, 1999. **82**(5): p. 944-947.

5.11. Qiao, P.Z., M.J. Yang, and F. Bobaru, *Impact mechanics and high-energy absorbing materials: Review.* Journal of Aerospace Engineering, 2008. **21**(4): p. 235-248.

5.12. Lee, J.H., et al., *Dynamic mechanical behavior of multilayer graphene via supersonic projectile penetration.* Science, 2014. **346**(6213): p. 1092-1096.

5.13. Davis, J.R., *Corrosion of aluminum and aluminum alloys*1999, Materials Park, OH: ASM International. vii, 313 p.

5.14. Lavernia, E.J., R.J. Perez, and J. Zhang, *Damping behavior of discontinuously reinforced Al alloy metal-matrix composites.* Metallurgical and Materials Transactions A, 1995. **26**(11): p. 2803-2818.

5.15. Jennett, N.M. and J. Nunn, *High resolution measurement of dynamic (nano) indentation impact energy: a step towards the determination of indentation fracture resistance.* Philosophical Magazine, 2011. **91**(7-9): p. 1200-1220.

5.16. Constantinides, G., et al., *Quantitative Impact Testing of Energy Dissipation at Surfaces.* Experimental Mechanics, 2009. **49**(4): p. 511-522.

5.17. Xia, X.H., et al., *Graphene Sheet/Porous NiO Hybrid Film for Supercapacitor Applications.* Chemistry-a European Journal, 2011. **17**(39): p. 10898-10905.

5.18. Tang, L.H., et al., *Uniform and rich-wrinkled electrophoretic deposited graphene film: a robust electrochemical platform for TNT sensing.* Chemical Communications, 2010. **46**(32): p. 5882-5884.

5.19. Lee, V., et al., *Large-Area Chemically Modified Graphene Films: Electrophoretic Deposition and Characterization by Soft X-ray Absorption Spectroscopy.* Chemistry of Materials, 2009. **21**(16): p. 3905-3916.

5.20. Hasan, S.A., et al., *Transferable Graphene Oxide Films with Tunable Microstructures.* Acs Nano, 2010. **4**(12): p. 7367-7372.

5.21. Ghosh, A., et al., *Characterization and assessment of localized dynamic deformation using nano-impact indentation.* 2015.

5.22. Sun, X.M., et al., *Monodisperse Chemically Modified Graphene Obtained by Density Gradient Ultracentrifugal Rate Separation.* Acs Nano, 2010. **4**(6): p. 3381-3389.

5.23. Arreguin-Zavala, J., et al., *Characterization of Nanostructured and Ultrafine-Grain Aluminum-Silicon Claddings using the Nanoimpact Indentation Technique.* Jom, 2013. **65**(6): p. 763-768.

CHAPTER 6

Summary

The following points summarize the previous chapters:

- From current density curves obtained at different voltages, deposition at all three applied potentials – 10 V, 15 V and 20 V – demonstrated well-controlled EPD process without reduction reaction or severe water hydrolysis observed in previous studies at the same potential. This suggests that reduction of graphene oxide (GO) during EPD process does not only depend on applied voltage but also on other parameters including solution concentration and liquid medium.

- Effect of deposition parameters on overall quality and microstructure of GO films was investigated. Increase in deposition time caused deterioration of deposited films due to bubble and wrinkle formations on the surfaces. The deposited GO sheets in general lied flat on the substrate surface with occasional wrinkles due to overlapping and distortion of carbon plane from oxygenated defects. The difference in area covered by wrinkles was statistically insignificant with respect to applied potential.

- Adhesion of GO films on three different Al alloy substrates – Al 1100, Al 5052, and Al 6061 – were qualitatively tested by q-tip rub and scotch tape peel. Elemental compositions significantly affected adhesion of the deposited GO films. GO films were well adhered to Al 1100 and Al 5052 substrates even after heat treatment at 150 °C. However, the films deposited on Al 6061 substrates were easily detached from the substrates.

- Chemical properties of EPD GO films on Al 1100 and Al 5052 substrates were studied using FT-IR and XPS depth profiling. The results proposed possible metal ion penetration into EPD GO films. Moreover, Al formed Al-O-C bonds with oxygenated defects on GO sheets rather than aluminum carbide formation. Peak shifts in Al 2p and

Mg 1s peaks were observed in heat-treated samples suggesting possible chemical structure change during removal of the defects.

- High-strain rate nano-impact tests were performed on GO films on Al 5052 substrates at various impact velocities. Obtained pendulum displacement curves displayed immediate damping of pendulum upon collision with thick GO films. In addition, specimens with thick GO films have shown more plastic collision characteristics with indenter tip compared to specimens with thin films and bare substrates. Overall, GO films demonstrated exceptional ability to dissipate dynamic impact energy per material density compared to Al alloy substrates.